Proceedings of the 18th Hellenic Nuclear Physics Society
Symposium 2009

Index table

18th Symposium of the Hellenic Nuclear Physics Society

N.C.S.R. Demokritos, 29-30 May 2009

PROGRAMME*
FRIDAY, 29 May 2009

Session I Chair: Pakou, Athena (U. Ioannina)

08.45 - 09.00 Opening

09.00 - 10.00 Casten, Richard F. (Yale U., U.S.A.)
Quantum phase transitions in nuclei: empirical signatures of collective structural evolution and its microscopic drivers.

10.00 - 10.20 Lalazissis, Georgios (U. Thessaloniki)
Relativistic density functionals for nuclear structure studies.

10.20 - 10.40 Kosmas, Theocharis (U. Ioannina)
The nucleus as a laboratory to study low-energy neutrino physics.

10.40 - 11.00 Fossion, Ruben (U. Nacional Autonoma de Mexico, Mexico)
Chaos in hadrons.

Session II Chair: Vlastou, Rosa (National Technical U. Athens)

11.30 - 11.50 Zamani-Valasiadou, Maria (U. Thessaloniki)
New experimental cross section data for transmutation and astrophysics applications.

11.50 - 12.05 Moustakidis, Charalambos (U. Thessaloniki)
Equation of state for dense supernova matter.

12.05 - 12.25 Souliotis, Georgios (Texas A&M, U.S.A., and U. Athens)
Studies of the nuclear landscape and the nuclear equation of state using peripheral collisions near the Fermi energy.

12.25 - 12.45 Veselsky, Martin (IP, SAS, Bratislava, Slovakia)
Isospin dynamics and production of exotic nuclei below 50AMeV.

12.45 - 13.00 Patronis, Nikolas (U. Ioannina)
Analysis of elastic backscattering and fusion data for 6,7Li + 28Si at sub- and nearbarrier energies: Probing the nuclear potential anomaly of weakly bound nuclei.

15.00- 16.00 Satellite meeting on Environmental Radioactivity

Session III Chair: Stiliaris, Efstathios (U. Athens)

15.00 - 15.15 Konstantinopoulos, Theodoros (INP, NCSR Demokritos)
128Xe lifetime measurement using the Coulex-plunger technique in inverse kinematics.

15.15 - 15.30 Zerva, K. (U. Ioannina)
Elastic backscattering measurements for 6,7Li + 28Si at sub- and near-barrier energies.

15.30 - 15.45 Tsiganis, Andreas (National Technical U. Athens)
Study of the 197Au(n,2n) reaction cross section.
15.45 - 16.00 Diakaki, Maria (National Technical U. Athens)
Study of the d+11B system differential cross sections for NRA purposes.

16.00 - 16.15 Foteinou, Varvara (INP, NCSR Demokritos)
Cross section measurements of d-induced reactions on lithium.

16.15 - 16.30 Provatas, Georgios (INP, NCSR Demokritos)
Proton elastic scattering differential cross section measurements of 45Sc.

17.00 - 19.00 General Assembly of the Hellenic Nuclear Physics Society

SATURDAY, 30 May 2009

Session IV Chair: Florou, Eleni (INT-RP NCSR Demokritos and U. Athens)

08.30 - 08.45 Aslanoglou, Xenofon (U. Ioannina)
The CASTOR calorimeter at CERN: Recent developments.

08.45 - 09.00 Savvidis, Ilias (U. Thessaloniki)
Underground low flux neutron background measurements in LSM using a large volume (1m3) spherical proportional counter.

09.00 - 09.15 Mikeli, Maria (U. Athens)
Scintillation crystals for gamma-camera imaging devices.

09.15 - 09.30 Ioannidou, Alexandra (U. Thessaloniki)
Activity size distribution of 7Be aerosols and their influence by air pollutants.

09.30 - 09.45 Tsabaris, Christos (Hellenic Centre for Marine Research)
The development and application of an autonomous in situ gamma-ray spectrometer for continuous radioactivity monitoring.

09.45 - 10.00 Bagatelas, Christos (Hellenic Centre of Marine Research)
Monte Carlo simulation of a NaI detector in the aquatic environment.

10.00 - 10.15 Patiris, Dionisis (U. Ioannina)
Detection of plated-out radon progenies on CR-39 detectors.

10.15 - 10.30 Sokaras, Dimosthenis (INP, NCSR Demokritos)
Measurement of the X-ray resonant Raman scattering cross section on aluminum.

10.30 - 10.45 Kantarelou, Vassiliki (INP, NCSR Demokritos)
Micro-XRF analysis of gilded bronze figurines at the national archaeological museum of Damascus.

Session V Chair: Ch. Moustakidis (U. Thessaloniki)

11.15 - 11.30 Anagnostatos, Gerassimos (INP, NCSR Demokritos)
Multi-harmonic shell model of nuclear structure.

11.30 - 11.45 Tarpanov, Dimitar (INRNE, BAS, Sofia, Bulgaria)
The effects of a tensor force on the single-particle evolution in Z=14 and N=28 chains.

11.45 - 12.00 Daoutidis, Ioannis (Technical U. Munich, Germany)
The relativistic RPA approach with exact coupling to the continuum.

12.00 - 12.15 Prassa, Vaia (U. Thessaloniki)
Kaon potentials in heavy ion collisions at intermediate energy.

12.15 - 12.30 Balasi, Konstantia (U. Ioannina)
Neutrino scattering off the stable even-even Mo isotopes.

12.30 - 12.45 Karathanou, Georgia (U. Ioannina)
Coherent scattering detection of 8B and hep solar neutrinos.

12.45 - 13.00 Tsakstara, Vaitsa (U. Ioannina)
Nuclear response to supernova neutrino spectra.

13.00 - 13.15 Stavrou, Vasilios (Hellenic Naval Academy) and Kardaras, Ioannis (U. Ioannina)
Nuclear muon capture rates by using relativistic muon wavefunctions.

13.15 - 13.30 Bonatsos, Dennis (INP, NCSR Demokritos)
A long sought result: Closed analytical solutions of the Bohr Hamiltonian with the Morse potential

13.30 Closing

***** Talks will take place in the amphitheater of the Institute of Materials Science.
Registration, coffee breaks, lunch, poster session will take place on the upper floor of the Tandem Accelerator Laboratory.

POSTERS

P01 Chatzisavvas, K. (U. Thessaloniki)
Complexity and neutron stars structure.

P02 Eleftheriadis, Konstantinos (INT-RP NCSR Demokritos)
Attachment coefficient of 211Pb on polydisperse aerosol.

P03 Eleftheriou, Georgios (Hellenic Centre of Marine Research)
Vertical distribution of 137Cs and natural radioactivity in core sediments of Thermaikos Gulf, northwestern Aegean Sea.

P04 Evangeliou, Nikolaos (INT-RP NCSR Demokritos and U. Athens)
The use of radionuclides 137Cs and 234Th in oceanographic research.

P05 Fragopoulou, Marianthi (U. Thessaloniki)
A neutron dosimeter of high sensitivity based on p-MOSFETs.

P06 Karatzikos, Stavros (U. Thessaloniki)
The fission barriers in actinides and superheavy nuclei in the covariant density functional theory.

P07 Manolopoulou, Metaxia (U. Thessaloniki)
Nonlinearity of recoil pulse height events in He-3 counters.

P08 Manousakas, Manousos-Ioannis (U. Patras)
Measurements of natural radionuclides in soil cores from the area of Megalopolis, Soutern Greece.

P09 Pavlou, Georgios (U. Athens)
A CBF calculation of $^1S_0$ superfluidity in the inner crust of neutron stars.

P10 Prospathopoulos, Aristides (Hellenic Centre for Marine Research)
A new method for automated analysis of in-situ NaI spectra in the marine environment based on discrete wavelet transform.

P11 Smponias, Theodoros (TEI of Western Macedonia, Kastoria)
Modelling neutrino emission from the jets in the SS433 microquasar

P12 Soupioni, Magdalini (U. Patras)
Bioaccumulation of heavy metals and 137Cs in Mytilus galloprovincialis from Galaxidi Gulf, Greece.

P13 Stamoulis, Kostas (U. Ioannina)
Determination of uranium and radium isotopes in water samples by liquid scintillation counting, using alpha/beta discrimination.

P14 Stoulos, Stilianos (U. Thessaloniki)
Indoor Radon source potential: Dose assessment on a model dwelling at temperate climate

Proceedings of the 18th Hellenic Nuclear Physics Society Symposium (2009)

Detection of plated-out radon progenies on CR-39 detectors

D.L. Patiris[a,b], K.G. Ioannides[b], C. Tsabaris[a]

[a] *Institute of Oceanography, Hellenic Center for Marine Research, 190 13 Anavyssos, Greece*

[b] *Nuclear Physics Laboratory, Physics Department, University of Ioannina, 451 10 Ioannina, Greece*

Abstract

A spectrometric study of alpha particles using CR-39 solid state nuclear track detectors is described. It is based on the application of software imposed selection criteria, concerning the geometrical and optical properties of the tracks which are created by alpha particles of specific energy falling on the detector at given angles of incidence. These selection criteria are based on a preliminary study of tracks' parameters (major and minor axes and mean value of brightness), using the TRIAC II code. Since no linear relation was found between the energy and the geometric characteristics of the tracks (major and minor axes), we resorted to the use of an additional parameter in order to classify the tracks according to the particles' energy. Since the brightness of tracks is associated with the tracks' depth, the mean value of brightness was chosen as the third parameter. This method could be applied as a low cost technique in studies concerning the radon's daughters ^{218}Po and ^{214}Po behavior in air.

Key words: Radon, polonium, radio-ecology, SSNTD, TRIACII.

1. Introduction

Radon and its polonium daughters (^{218}Po, ^{214}Po and ^{210}Po) are alpha particle emitters. Solid state nuclear track detectors are widely [1] used in radon measurements through the detection of the emitted alpha particles. The number of tracks recorded per unit area provides information on the radon radioactivity concentration of the investigated environment. Although this information is valuable for radiological studies, counting only the total number of tracks is not useful to differentiate these radioisotopes and thus study their behaviour. However, the tracks' geometrical and optical characteristics convey information on the particles' energy and angle of incidence. Following a standard chemical etching procedure, the shape of the created tracks in the special case of vertical particle incidence is circular, whilst it is elliptical in the general case. The size of the tracks depends both upon the energy and the angle of incidence. Geometrical models concerning the growth of the tracks' length predict that there is no linearity between the axis (major and minor) of elliptical tracks

and the particles' energy. As a result, the identification of radon daughters with an alpha spectrometric method, based on the use of SSNTDs is not a trivial task [2–9].

In the present work, using the TRIAC II code [10], a comprehensive study of the major axis, the minor axis and the mean value of tracks' brightness is presented. The results verify in agreement with previous research [11–14], the geometrical models' predictions, showing the absence of a linear relation between the tracks' openings with energy. The behaviour of those parameters was investigated for a wide range of particles' incidence angles and for different chemical etching durations, ranging from 6 up to 14 h. As it will be elucidated below, increasing the etching time, the elliptical tracks' shape gradually converts to circular and a linear relation between the mean values of brightness with energy can be established. Although this is an important finding, which can be applied for spectrometry, etching for 14 h or more outgrows tracks and the resulting overlapping hinder the schematic differentiation of the tracks. Even when an image analysis program, which can analyze overlapping tracks, is used, the overlap of tracks sets an upper limit to the measurement of the surface concentration of the tracks, approximately 250 tracks/mm2. Outgrown overlapped tracks create a continuous band, thus an accurate estimation of the geometrical parameters is impractical. Finally, using the results of tracks' parameters analysis, a method to separate the tracks of deposited on the detectors ^{218}Po and ^{214}Po is proposed. Deposition is one of the main removal mechanisms of airborne aerosol particles in addition to ventilation and decay for radioactive aerosols. While ventilation and decay are well understood and usually easy to quantify, the understanding of the deposition process is still not adequate. Moreover, deposition depends on the properties of the aerosol particles such as size, charge, shape and condition of internal surfaces and also on air flow. The method described here is a method for the direct detection and differentiation of deposited radon's progeny and it could be applied as an inexpensive tool to the understanding of the deposition processes and the behaviour of radioactive aerosols.

2. Experimental methods.

The CR-39 detectors used in the present study were supplied by Pershore Mouldings Ltd. (Worcestershire, UK), with a nominal thickness of 1000 μm. The cut detectors (1x10 cm^2) were systematically irradiated inside a vacuum chamber (10^{-2} torr) with alpha particles and energies ranging from 1.5 MeV to 5.5 MeV. An americium (^{241}Am) source (main energy 5.48 MeV) was employed in combination with number of energy absorbers. The detector irradiation setup consisted of a source mounting, an absorber holder and a narrow cylindrical tube made of Plexiglas acrylic material, acting as a beam collimator. The collimator was placed on a rotator, with the exit a few millimetres close to CR-39 detector. Rotating the collimator, the angle of incidence to the detector's surface was varied from 90^o (vertical incidence) up to 35^o, in steps of 5^o. As it was found after some test runs, no tracks were recorded for angles smaller than 45^o and chemical etching times up to 8 h. Angles of incidence smaller than 45–40^o are close to the critical (or registration) angle. This is the minimum angle of incidence with respect to the detector's surface in which tracks can be formed by the chemical etching

of the detectors. The initial energy of the alpha particles was reduced by absorbers. Three different materials (kapton, polyethylene, aluminium) were used in the form of thin foils. The energy of the particles falling on the detector's surface was determined by an alpha spectroscopy system based on a surface barrier silicon detector. The detectors were etched in a 6 N aqueous NaOH solution, maintained at 75° C in a water bath with a temperature control better than 1° C. Following the first 6h of etching, the detectors were removed from the etchant, were rinsed with de-ionized water and finally they were dried in an oven at 50° C overnight. Then a number of images of the detectors' surfaces were captured with the use of a microscope – video camera – frame grabber – computer recording arrangement. For each combination of energy-angle-chemical etching duration, a number of 200–400 tracks were analyzed from three CR-39 detectors, thus achieving adequate statistics. Following the completion of the image acquisition step, the same detectors were etched for another hour and their tracks were again recorded and analyzed. This procedure was repeated until the detectors' etching time totaled 14 h.

3. Results and discussion.

3.1. Spectrometric study.

The association between the geometrical characteristics (major axis indicatively) of the tracks and the energy of the alpha particles for different etching times is presented in figure 1. The parameters of major and minor axis did not correlate with the energy of the particles for all angles of incidence. It is notable that after the first steps of etching (6–7 h), wider tracks are created by particles of lower energies. However, this feature is not sufficient for classifying tracks according to their energy. For example, particles with the energy of 5.5 MeV, which impact vertically onto the detector's surface, produce tracks with the same value of major (or minor) axis as the particles of lower energy do, when they collide with the detector at smaller angles of incidence. Moreover, as the

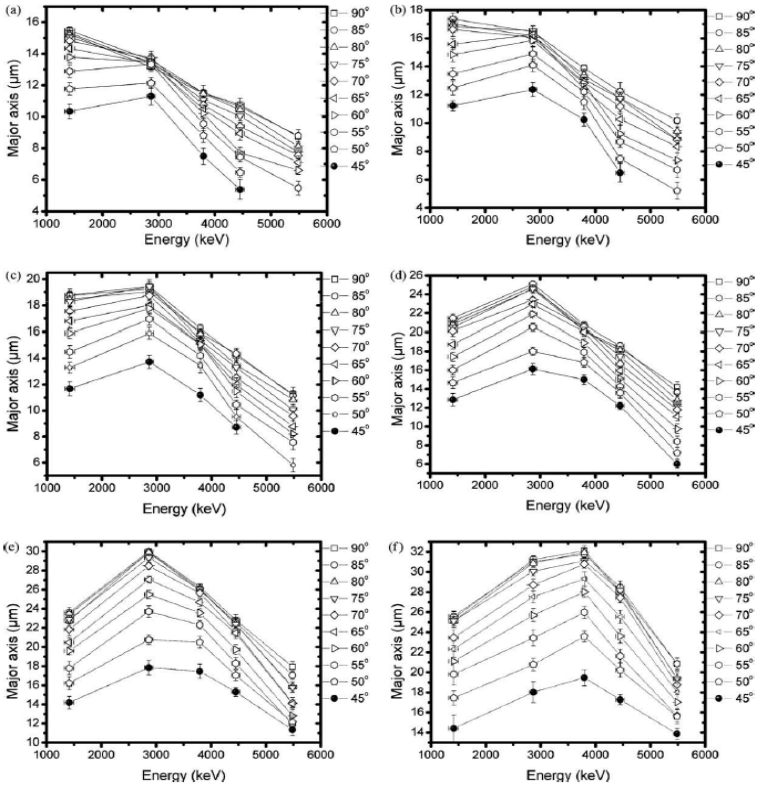

Figure 1: The relation between the major axis and the particles' energy for etching duration: (a) 6 h, (b) 7 h, (c) 8 h, (d) 10 h, (e) 12 h, (f) 14 h.

duration of the etching process is increased, particles with greater energies gradually produce wider tracks' sizes, however more particles with different energies and (or) angles of incidence concurrently register into tracks with the same value of major and minor axis. The visualization of tracks is carried out by placing the detector between the source of light and the microscope's objective lens. A ray of light transverses the detector following a straight line trajectory, which is redirected, when it is refracted out in air. The change in direction is due to the change of the optical medium and depends on the angle of refraction. Since there is not a preferred angle, the total contribution to the brightness of the optical field is almost uniform. However if before exiting, a light ray enters a region where a track was developed, a series of optical phenomena like refractions and reflections affect its final deflection. This is the reason explaining why the particles' tracks seem darker from the detector's surface and can be recognized from the background of the image. To study the brightness of the tracks, the mean value of tracks' brightness was estimated by the TRIAC II program for all the combinations of incident particle energies-angles and chemical etching durations. The association between the mean brightness of the tracks and the alpha particles' energy for different angles of incidence and etching durations is presented graphically in figure 2. Following digitalization, brightness was expressed by a value in the range 0–255. A brightness value of 0 corresponded to total black, while a value of 255 represented maximum illumination of the optical field. Then, as the duration of etching is increased, the tracks from particles with greater energies register darker. After 14 h of etching, a close to linear relation between brightness and particles' energy, referred to the same angle of incidence was found. Taking into account the evolution of this parameter with etching, additional etching was found to improve the linearity. Although this finding is important for spectrometric purposes, the outgrowth of tracks sets an upper limit to the tracks' surface concentration. For our experimental setup, this limit was 250 tracks mm^{-2}. More tracks would lead to an extensive overlapping of the tracks, thus affecting the accuracy of the measurements.

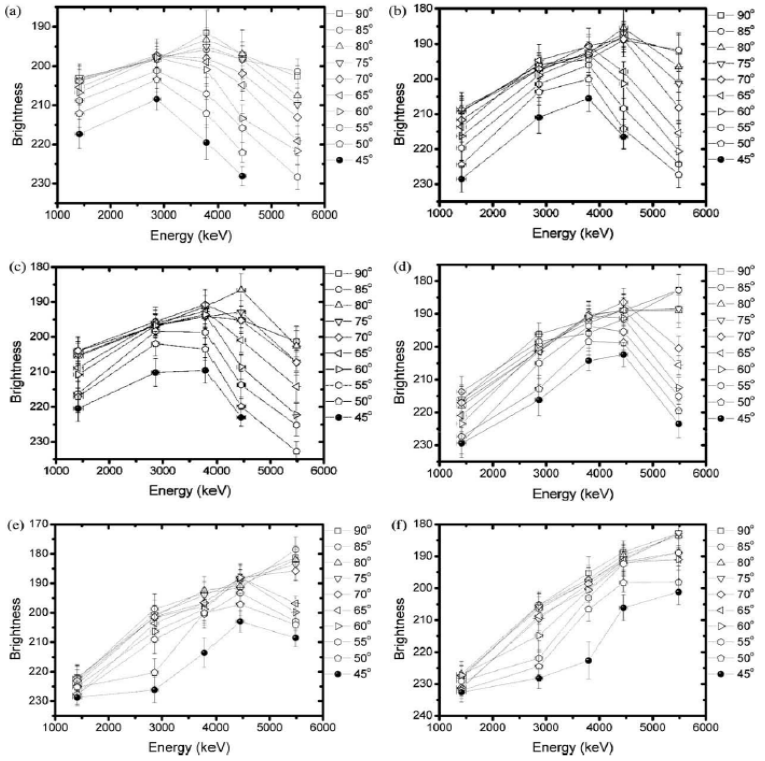

Figure 2: The relation between the brightness and the particles' energy for etching duration: (a) 6 h, (b) 7 h, (c) 8 h, (d) 10 h, (e) 12 h, (f) 14 h.

3.2. The discrimination of deposited ^{218}Po and ^{214}Po, as an application of the spectrometric study.

As an application of the described spectrometric study, a method of direct detection and separation of the deposited radon's progeny ^{218}Po and ^{214}Po was tested. After the generation of radon's daughters in air, these isotopes are found at three states, as attached to atmospheric aerosols, as unattached (free) and as deposited nuclei on available. Their deposition is an important removal process and many studies concerning the estimation of the portion of the deposited progeny have been proposed. The method, which is proposed in the present study, depends on the direct detection of deposited isotopes ^{218}Po and ^{214}Po, considering as deposition surface, the surface of CR-39 detectors and using the results of the spectrometric analysis. The radon progeny, deposited on the detector's surface emit alpha particles, which impact on the detector with their entire energy; in particular, ^{218}Po emits alpha particles with initial energy of 6.0 MeV and ^{214}Po particles with initial energy of 7.7 MeV. A number of experimental problems had to be solved since our experimental data were ranging between 1.5 MeV and 5.5 MeV. An approach to overcome these complications was to shield the detectors with an appropriate absorber so to reduce the particles energy. A number of calculations were performed using the code SRIM to determine the kind and the thickness of the absorber material. An aluminium foil of 15 μm thickness was found optimal for our purpose. Close enough; the thickness of the commercially available aluminium foils was estimated equal to 14.2 μm. This absorber reduces the energy of the emitted particles from ^{218}Po to 3.6 MeV and from ^{214}Po to 5.8 MeV.

Two CR-39 detectors, one of them covered with commercial aluminium foil, were placed for 60 h inside a non ventilated chamber, with a volume of 67 L, together with a ^{226}Ra radioactive source of 4000 Bq activity. To monitor the exposure of CR-39 detectors, a Continuous Air Monitoring (CAM) PIPS detector was placed inside the chamber, capable to operate under environmental conditions. The spectra from this detector, acquired using standard electronics were analysed to validate the results of the proposed method. Following the exposure in the radon rich environment, the CR-39 detectors were etched in a 6 N aqueous NaOH solution, maintained at 75^{o} C for 8 h. A number of images containing a total of 3500 tracks from each detector was scrutinised by the TRIAC II program. The results of the analysis are presented in figure 3. The energy spectrum of the detected alpha particles accumulated using the CAM-PIPS detector is presented in Fig. 3(a). This is

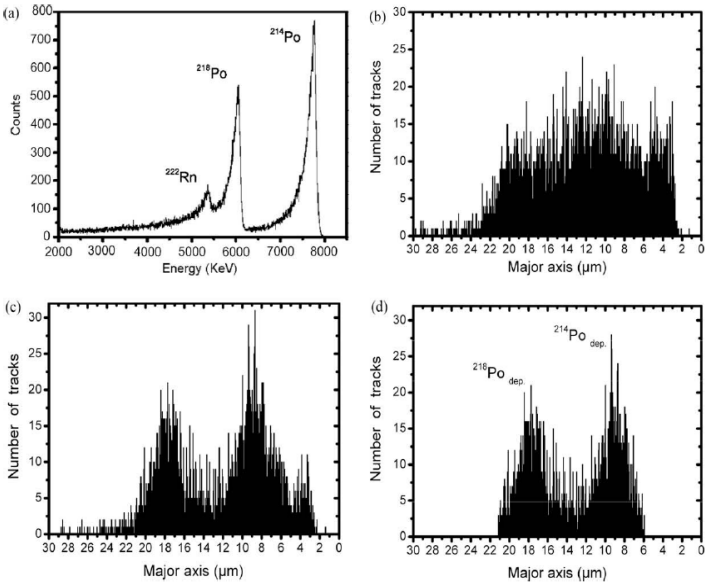

Figure 3: The results of the exposure to a radon rich air environment.

a typical radon environment spectrum, where the deposited progeny onto the detector's surface produce two well separated peaks, while radon, remaining free in air, emits alpha particles from a region around the detector, producing a continuous spectrum up to 5.5 MeV. Histograms of the measured major axis values from the registered CR-39 detector tracks are also presented for the uncovered detector (Fig. 3(b)) and for the covered with the absorber detector, before (Fig. 3(c)) and after (Fig. 3(d)) the application of the energy selection criteria. Comparing the histograms derived from the uncovered and the covered detectors, two groups of values for the major axis are recognized from the uncovered detector tracks. This is due to the deposition of the polonium isotopes onto the absorber surface in combination with the appropriate kind and thickness of the absorber, which allow the formation and recognition of tracks from particles of those isotopes under the chosen chemical etching conditions. The histogram of Fig. 3(c) was obtained by all the recognised tracks and neither selection criteria nor other discriminative procedure was applied. After imposing the selection criteria, the noticeable regions remain, providing an evidence of the radon's progeny differentiation.

4. Conclusions

The method described here for the detection and differentiation of the alpha emitter radon's progeny (^{218}Po and ^{214}Po) was based on the spectrometric analysis of the geometrical and optical characteristics of the particles' tracks. This study focused on the CR-39 solid state nuclear track detector has shown the absence of a linear relation between both major and minor axis of the tracks with the particles' energy. Instead, a linear relation between the mean value of brightness and energy is established after a prolonged chemical etching (greater than 14 h). The usage of this finding is limited by the maximum surface concentration of the tracks, due to tracks overlapping.

References

[1] V.A. Nikolaev, R. Ilic, Radiat. Measur. 30 (1999) 1.
[2] A.P. Fews, Nucl. Instr. and Meth. B 72 (1992) 91.
[3] A.M. Abdel-Moneim, A. Abdel-Naby, F.A. El-Akka, Nucl. Tracks Radiat. Mess. 21(1993) 235.
[4] O.A. Bondarenko, P.L. Salmon, D.L. Henshaw, A.P. Fews, A.N. Ross, Nucl. Instr. Meth. A 396 (1996) 582.
[5] P. Mozzo, F. Trotti, A. Temporin, M. Lanciai, F. Predicatori, F. Righetti, A. Tacconi, Environ. Inter. 22 (1996) 595.
[6] M. El Hofy, H. El Samman, W. Arafa, Radiat. Measur. 31 (1999) 241.
[7] A. Boukhair, A. Haessler, J.C. Adloff, A. Nourreddine, Nucl. Instr. and Meth. B 160 (2000) 550.
[8] Z. Lounis, S. Djeffal, K. Morsli, M. Allab, Nucl. Instr. and Meth. B 179 (2001) 543.
[9] A.A.R. Da Silva, E.M. Yoshimura, Radiat. Measur. 39 (2005) 621.
[10] D.L. Patiris, K. Blekas, K.G. Ioannides, Comput. Phys. Commun. 177 (2007) 329.
[11] D. Nikezic, D. Kostic, C.W.Y. Yip, K.N. Yu, Radiat. Measur. 41 (2006) 253.
[12] B. Dörschel, D. Hermsdorf, U. Reichelt, S. Starke, Y. Wang, Radiat. Measur. 37 (2003) 563.
[13] B. Dörschel, D. Hermsdorf, U. Reichelt, S. Starke, Radiat. Measur. 37 (2003) 573.
[14] M. Fromm, F. Membrey, A. Chambaudet, R. Saouli, Nucl. Tracks Radiat. Measur. 19 (1991) 163.

^{128}Xe Lifetime Measurement Using the Coulex-Plunger Technique in Inverse Kinematics

T. Konstantinopoulos [a], A. Lagoyannis [a], S. Harissopulos [a], A. Dewald [b], W. Rother [b], G. Ilie [b], R. Julin [c], P. Jones [c], P. Rakhila [c], P. Greenlees [c], T. Grahn [c] and D. L. Balabanski [d]

[a] *Institute of Nuclear Physics, National Centre for Scientific Research "Demokritos",15310 Aghia Paraskevi, Athens, Greece*

[b] *Institut för Kernphysic, Universität zu Köln, Zülpicherst, 77, D-50937 Köln, Germany*

[c] *Department of Physics, University of Jyväskylä, P.O. Box 35, 40014 Jyväskylä, Finland*

[d] *INRNE, Sofia, Bulgaria*

Abstract

The lifetimes of the lowest collective yrast and non-yrast states in ^{128}Xe were measured in a Coulomb excitation experiment using the recoil distance method (RDM) in inverse kinematics. Hereby, the Cologne plunger apparatus was employed together with the JUROGAM spectrometer. Excited states in ^{128}Xe were populated via projectile Coulomb excitation in inverse kinematics, i.e. by using a ^{128}Xe beam impinging on a ^{nat}Fe target at E (^{128}Xe) $\sim$ 525 MeV. Recoils were detected by means of an array of solar cells placed at forward angles. Recoil-gated -spectra were measured at different plunger distances.

Preprint submitted to Elsevier *30 April 2011*

Experimental study of the ^{197}Au(n,2n) reaction cross section

A. Tsinganis[a], M. Kokkoris[a], A. Lagoyannis[b], E. Mara[a], C. T. Papadopoulos[a], R. Vlastou[a]

[a] *Department of Physics, National Technical University of Athens, Greece*
[b] *Institute of Nuclear Physics, NCSR "Demokritos", Athens, Greece*

Abstract

In the present work, the ^{197}Au(n,2n) reaction cross section is experimentally determined relative to the ^{27}Al(n,α)^{24}Na reaction at incident neutron energies of 9.0 to 10.5 MeV by means of the activation technique. The quasi-monoenergetic fast neutron beam was produced via the ^{2}H(d,n)^{3}He reaction at the 5.5 MV Tandem Van de Graaff accelerator at the NCSR "Demokritos" and was studied to determine the contribution of background "parasitic" neutrons using the multiple foil activation technique and the SULSA unfolding code. The cross sections for the population of the second isomeric state (12^-) of ^{196}Au and the sum of the ground (2^-) and first isomeric state (5^-) population cross sections were independently determined. Auxiliary Monte Carlo simulations were performed with the MCNP code.

1. Introduction

The presence of a high spin isomeric state in the residual nucleus of a neutron threshold reaction provides a sensitive test for existing nuclear models. The systematic study of the excitation function of the formation of both the ground and the high spin isomeric state on the basis of a statistical model provides information on the energy and spin distribution of the level density of the nuclei involved [1] and on the changes in the structure of the low lying excited states of the corresponding nuclei.

In this context the ^{196}Au isotope presents an interesting isomeric pair: ground and isomeric states with spin values of 2^- and 12^- respectively (Fig. 1). This 12^- isomer has been reported for other even A Au isotopes (^{198}Au, ^{200}Au) [2]. However, a survey of the literature revealed only a limited number of experimental data for the cross section of the ^{197}Au(n,2n)^{196}Au^{m2} reaction, especially near its threshold, where only one unpublished dataset [3] was found.

Thus, the purpose of this work was to experimentally determine the ^{197}Au(n,2n)^{196}Au^{m2} and the ^{197}Au(n,2n)^{196}Au^{g+m1} reaction cross sections in the incident neutron energy range between 9 and 10.5 MeV, i.e. close to the threshold, by means of the activation technique, with the view of conducting a detailed theoretical study of these cross-sections in the near future.

2. Experimental

2.1. Irradiations

Four irradiations have been carried out, evenly spaced in the energy range between 9.0 to 10.5 MeV. Given that the cross section for the formation of the second isomeric state is significantly lower than that for the population of the ground state, the irradiations typically lasted approximately 24 hours, which corresponds to roughly 84% of the saturated activity of the second isomeric state.

High purity natural gold foils (99.99% ^{197}Au) with a diameter of 14 mm and thickness of 0.5 mm were used. Two Al foils of the same diameter and thickness were placed immediately before and after the gold foil and were used to determine the neutron flux.

The quasi-monoenergetic neutron beam was produced via the ^{2}H(d,n)^{3}He reaction by bombarding a deuterium gas target with a deuteron beam at currents around 1-2 μA. The gas target is fitted with a 5 μm molybdenum entrance foil and a 1 mm Pt beam stop and is constantly cooled with a cold air jet during

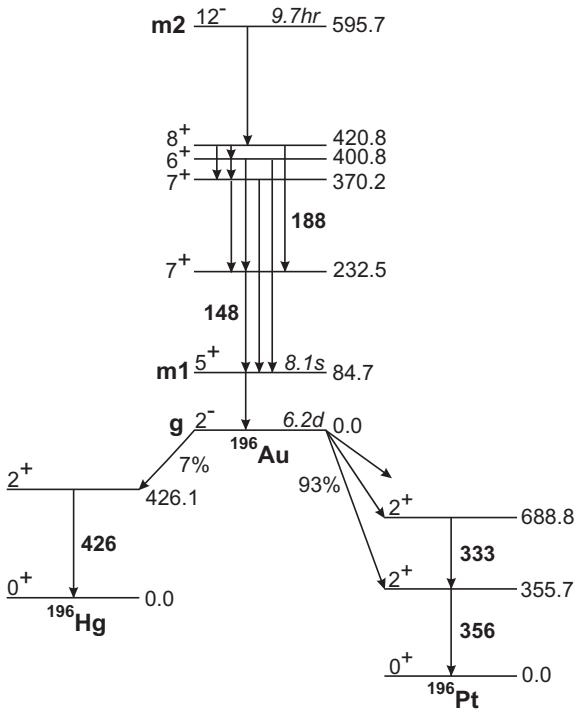

Figure 1: Simplified decay scheme of the isomeric and ground states of the residual nucleus ^{196}Au. All energies are given in keV.

irradiation to diminish the risk of damage to the Mo foil. The deuterium pressure was set to 1500 mbar. Using this setup, the achieved flux varied between 3×10^5-4×10^6 n/(cm^2·s) in the four runs performed.

The samples were placed at 0° with respect to the neutron beam and at a distance of 8 cm from the center of the gas cell, thus limiting the angular acceptance of the target foils to ±5°.

Beam fluctuations were monitored with a BF_3 counter placed at a distance of 3 m from the deuterium gas target. Following Monte Carlo simulations of the experimental area, the BF_3 unit was placed at an angle of 30° with respect to the beam line to avoid an increased presence of "parasitic" background neutrons near the target foils due to backscattering on the BF_3 setup. Data from the BF_3 counter were stored at regular time intervals (60 s) by means of a multi-channel scaler and were used to correct for the decay of ^{196}Au nuclei during irradiation and to account for fluctuations in the beam flux in the subsequent off-line analysis.

2.2. Neutron Beam

Particular attention was given to estimating the neutron energy distribution in the samples. The linearity of the selection magnet has been verified at low energies through the Al(p,γ) strong resonance at 991.91 keV and the ^{16}O(d,n) threshold reaction (E_{th}=1828.83 keV) leading to an estimate of the beam energy offset of 1.6 keV and a beam energy uncertainty of 0.1%. Assuming possible non-linearity at high energies, an overestimated beam energy uncertainty of 0.15% has been accepted to include possible second order effects.

A considerably more significant effect on the energy uncertainty of the produced neutrons is straggling from energy loss in the entrance foil and the deuterium target. Furthermore, as it was not possible to control the flow of deuterium in the gas cell remotely, the pressure was at times lower than the desired value by up to 200-300 mbar. These effects were estimated with the SRIM software [4] and the energy uncertainty value from straggling was less than 30keV. Finally, the angular acceptance of the target foils introduces additional uncertainty due to the ^{2}H(d,n)^{3}He reaction kinematics.

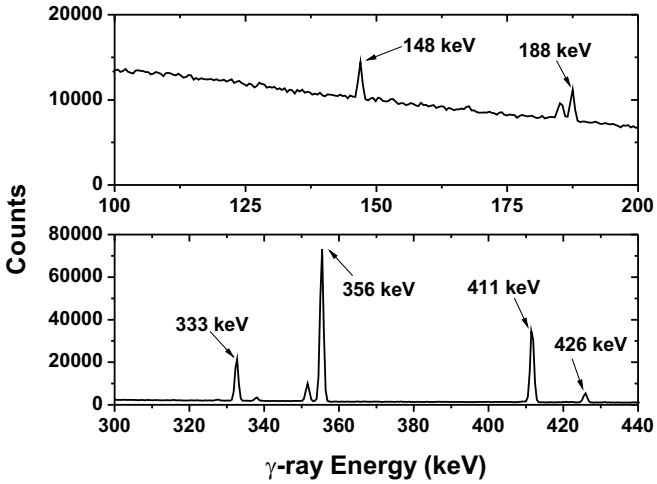

Figure 2: Experimental spectra from the decay of the second isomeric state (top panel) and ground state (bottom panel) of ^{196}Au, after irradiation at 10.5 MeV incident neutron energy. The acquisition time is 20hr and 51hr respectively.

Taking the above into account, the appropriate adjustments were made, where possible, to ensure that the width of the neutron energy distribution in the samples did not exceed 50keV.

The contribution of background "parasitic" neutrons was also studied in detail. These neutrons originate from the interaction of the deuteron beam with the beam line structural materials, beam collimators and gas cell components. The multiple foil activation technique was implemented to determine the neutron beam profile. The appropriate foils (Ni, Co, Ti, In, Zn, Fe, Nb) were chosen in which neutron threshold reactions take place at different threshold energies and they were placed immediately after the Au and two Al foils for irradiation. Information from the Au and Al foils was also included in this analysis.

The results of these irradiations were processed with the SULSA unfolding code [5]. By providing the activation rates measured for each foil, the code extrapolates the energy distribution of the beam using cross section values and covariance matrices from an incorporated library. Modifications were made to include additional reactions in the analysis.

The results of this analysis showed that, although a considerable population of background neutrons is produced during the irradiations, these lie mainly in the low-energy region, well below the threshold for the ^{197}Au(n,2n) (E_{th}= 8.11 MeV) reaction. As far as the ^{27}Al(n,α)^{24}Na reference reaction is concerned, while E_{th}= 3.25 MeV, the cross section only grows sufficiently to produce measurable activation rates at incident neutron energies above 6.8 MeV.

2.3. Activity Measurements

Following the irradiations, the induced activity on the samples was measured with a 56% relative efficiency HPGe detector. The detector was calibrated with ^{152}Eu and ^{207}Bi sources, the latter being used to obtain a more accurate efficiency curve in the low-energy region. The samples were placed at a distance of 10 cm from the detector window. With this counting setup, corrections for coincidence summing become negligible. Figure 2 shows typical spectra acquired from the gold samples during the measurement for the second isomeric state (top panel) and the ground state (bottom panel), where the γ-rays of interest have been marked.

The population of the second isomeric state was measured through the 148 keV line. This was preferred over the 188 keV line due to its higher intensity (45% over 30%) and the existence of a nearby natural background line (Fig. 2). These measurements began approximately 1 hr after the end of the irradiation and lasted up to 20 hr (two half-lives), depending on the evolution of the peak-to-background ratio. Following this, the activity of the Al foils was measured with the same experimental setup through the 1369 keV transition. For these measurements, a duration between 1 and 3 hr was sufficient to achieve a statistical error lower than 2%.

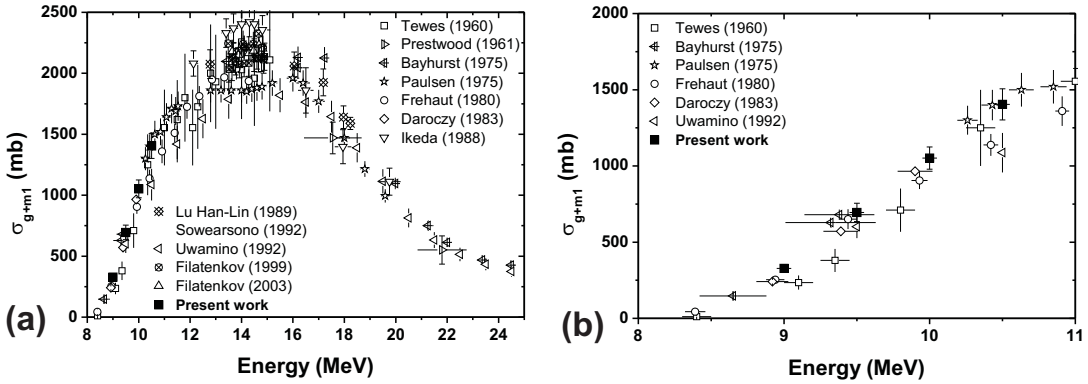

Figure 3: Experimental cross section values for the population of the ground and first isomeric state of ^{196}Au (g+m1) between 8-25 MeV (a) and 8-11 MeV (b). Several single-point datasets around 14 MeV omitted for clarity.

Since the first isomeric state decays relatively very quickly ($T_{1/2} = 8.1$ s), the measurements on the decay of the ground state result in the determination of the sum of the cross sections for the population of the ground state and the first isomeric state. Moreover, these measurements were carried out at least two days after the irradiation to ensure that the second isomeric state ($T_{1/2} = 9.6$ hr) had fully decayed to the ground state, since the correction for the contribution of the second isomeric state to the measured activity of the ground state was found to be negligible when the latter measurement was carried out after several half-lives of the second isomeric state.

The activity of the ground state was deduced through the 356 keV line, preferred over the 333- and 426 keV lines due to the much higher counting statistics (Fig. 2). Furthermore, the 333 keV line is contaminated by the 334 keV line of ^{198}Au arising from the ^{197}Au(n,γ)^{198}Au reaction. This is confirmed by the 411 keV line which is clearly visible in the acquired spectrum and also belongs to the (n,γ) channel.

3. Data Analysis

In each case, the experimental values of the cross sections were determined through the following formula:

$$\sigma = \frac{N_\gamma}{\epsilon I N_T \Phi S f D} \tag{1}$$

where N_γ is the number of counts in the relevant γ-ray peak. The factor ϵ is the detector efficiency, I is the γ-ray intensity, N_T is the number of target nuclei and S is the self-absorption correction factor. Decays during irradiation and time fluctuations in the beam flux are accounted for with the correction factor f, given by:

$$f = \frac{\int_0^{t_b} e^{-\lambda t} F(t)\, dt}{\int_0^{t_b} F(t)\, dt} e^{-\lambda t_b}, \tag{2}$$

where t_b is the irradiation time and $F(t)$ is the beam flux in arbitrary units as given by the BF_3 counter, while D corrects for the interval between the end of the irradiation and the end of the measurement and is given by:

$$D = (1 - e^{-\lambda t_m}) e^{-\lambda t_w}, \tag{3}$$

where t_w and t_m are the waiting time between irradiation and measurement and the measurement time respectively.

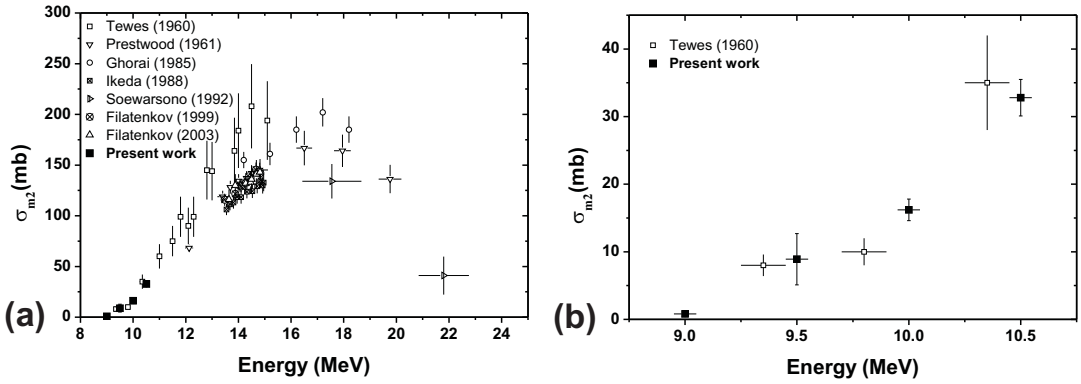

Figure 4: Experimental cross section values for the population of the second isomeric state of ^{196}Au (m2) between 8-25 MeV (a) and 8.5-11 MeV (b).

Table 1: Experimental cross section values for the ^{197}Au(n,2n)^{196}Au^{g+m1} and ^{197}Au(n,2n)^{196}Au^{m2} reactions and the isomeric cross section ratio

Energy (MeV)	σ_{g+m1} (mb)	σ_{m2} (mb)	$\sigma_{m2}/\sigma_{g+m1}$
9.0	328±26	0.8±0.1	0.0024±0.0003
9.5	695±60	8.9±3.8	0.013±0.006
10.0	1052±73	16.2±1.6	0.015±0.002
10.5	1404±102	32.8±2.7	0.023±0.003

The integrated neutron flux Φ was determined through the same formula (Eq. 1) by using the cross section values for the ^{27}Al(n,α)^{24}Na reaction found in literature [6] and by averaging over the deduced values in the front and back Al foils. It is thus possible to correct for target geometry and self-shielding.

Given the relatively low energy of the γ-rays of interest and the high mass attenuation coefficient of gold, it was essential to take self-absorption effects into consideration. A Monte Carlo simulation of the counting geometry using the MCNP code [7] was performed to estimate this correction. Approximately 55% of the 148 keV and 12% of the 356 keV line are lost due to self-absorption in a 0.5 mm -thick gold foil. Self-absorption of the 1369 keV line in Al was found to be less than 0.5%.

4. Results and Discussion

The experimental results of this work are presented in Table 1 along with their uncertainties. As seen in figure 3, the data for the ^{197}Au(n,2n)^{196}Au^{g+m1} cross section are in good agreement with previous measurements.

For the second isomeric state, only one previous dataset exists in the energy region from threshold to 13 MeV, contained in an unpublished report [3]. It has been impossible to obtain relevant information on the particular experiment, such as beam parameters, flux, irradiation intervals and the detector(s) used for the off-line measurements. A dataset of evaluated data in this region can additionally be found in [8], also an unpublished report. The new data presented in this work report significantly lower uncertainties (10-11% for the 10.0 and 10.5 MeV measurements compared to 20% in the other data within this range), barring the non-optimal 9.5 MeV measurement. Moreover, the measurement at 9.0 MeV is the only one carried out at this energy, so close to the threshold. The uncertainty in the incident neutron energy has also been reduced compared to the previous data, as described in subsection 2.2.

5. Conclusions

The cross section of the (n,2n) reaction on ^{197}Au, was measured independently for the population of the second isomeric state (σ_{m2}), and for the sum of the reaction cross section for the population of the ground and the first isomeric state (σ_{g+m1}). The cross section values were determined by means of the activation technique in the incident neutron energy range 9.0-10.5 MeV. The present data provide more accurate measurements in the near-threshold region.

6. Acknowledgments

The present work was partially supported by the NTUA program for fundamental research PEVE-2008. The authors would also like to acknowledge the assistance of the accelerator staff at NCSR "Demokritos".

[1] Y. P. Gangrsky, N. N. Kolesnikov, V. G. Lukashik, and L. M. Melnikova, Physics of Atomic Nuclei **67**, 1227 (2004).

[2] E. Hagn and E. Zech, Nucl. Phys. A **373**, 256 (1982).

[3] H. A. Tewes, A. A. Caretto, A. E. Miller, and D. R. Nethaway, Tech. Rep. 6028 (USA, 1960) data retreived from EXFOR: www-nds.iaea.org/exfor.

[4] J. F. Ziegler, J. P. Biersack, and U. Littmark, *The Stopping and Range of Ions in Solids* (Pergamon Press, New York, 1985).

[5] S. Sudar, *A Solution for the Neutron Spectrum Unfolding Problem without Using Input Spectrum*, Tech. Rep. INDC(HUN)-026/L (Vienna, 1989).

[6] A. Carlson, R. Block, J. Briggs, E. Cheng, H. Huria, M. Zerkle, K. Kozier, A. Courcelle, V. Pronyaev, and S. van der Marck, Nuclear Data Sheets **107**, 2391 (2006).

[7] F. B. Brown, R. F. Barrett, T. E. Booth, J. S. Bull, L. J. Cox, R. A. Forster, T. J. Goorley, R. D. Mosteller, S. E. Post, R. E. Prael, E. C. Selcow, A. Sood, and J. Sweezy, Trans. Am. Nucl. Soc. **87**, 273 (2002).

[8] C. Phillis and O. Bersillon, Tech. Rep. 4826 (France, 1977) data retrieved from EXFOR: www-nds.iaea.org/exfor.

A long sought result: Closed analytical solutions of the Bohr Hamiltonian with the Morse potential

Dennis Bonatsos [a], I. Boztosun [b], I. Inci [b]

[a] *Institute of Nuclear Physics, N.C.S.R. "Demokritos", GR-15310 Aghia Paraskevi, Attiki, Greece*

[b] *Department of Physics, Erciyes University, Kayseri, Turkey*

Abstract

Closed analytical solutions of the Morse potential for nonzero angular momenta has been an open problem for decades, solved recently by the Asymptotic Iteration Method (AIM) for solving differential equations. Closed analytical expressions have been obtained for the energy eigenvalues and B(E2) rates of the Bohr Hamiltonian in the γ-unstable case, as well as in an exactly separable rotational case with $\gamma \approx 0$, called the exactly separable Morse (ES-M) solution. All medium mass and heavy nuclei with known β_1 and γ_1 bandheads have been fitted by using the two-parameter γ-unstable solution for transitional nuclei and the three-parameter ES-M for rotational ones. It is shown that bandheads and energy spacings within the bands are well reproduced for more than 50 nuclei in each case. Comparisons to the fits provided by the Davidson and Kratzer potentials, also soluble by the AIM, are made.

The recent introduction of the critical point symmetries E(5) [1] and X(5) [2], which describe shape phase transitions between vibrational and γ-unstable/prolate deformed rotational nuclei respectively, has stirred much interest in special solutions of the Bohr Hamiltonian, describing collective nuclear properties in terms of the collective variables β and γ. Such solutions can describe nuclei in the whole region between different limiting symmetries, while critical point symmetries are appropriate for describing nuclei only at or near the critical point, in good agreement with experiment [3].

It has been known for a long time [4] that simple special solutions of the Bohr Hamiltonian, resulting from exact separation of variables in the relevant Schrödinger equation, can be obtained in the γ-unstable case, in which the potential depends only on β, as well as in the case in which the potential can be written in the separable form $u(\beta,\gamma) = u(\beta) + u(\gamma)/\beta^2$, in the special cases of $\gamma \approx 0$ or $\gamma \approx \pi/6$ [5]. An approximate separation of variables has also been attempted for potentials of the form $u(\beta,\gamma) = u(\beta) + u(\gamma)$ in the cases of $\gamma \approx 0$ [2] or $\gamma \approx \pi/6$ [6]. Sev-

eral special solutions involving different potentials (infinite well, harmonic oscillator, Coulomb, Kratzer, Davidson) have been worked out (see [7, 8] and references therein).

The potentials mentioned above are known to be exactly soluble for all values of angular momentum L. In the present work, we introduce special solutions for the Morse potential, $u(\beta) = e^{-2a(\beta-\beta_e)} - 2e^{-a(\beta-\beta_e)}$, which is known [9, 10] to be exactly soluble only for $L = 0$. The overall factor D of the Morse potential is set equal to unity, without affecting the method of solution, since it can be scaled out if ratios of energies are used, as in the present work. Analytical expressions for the spectra for any L are obtained by solving the relevant differential equation through the Asymptotic Iteration Method (AIM) [11,12], after applying the Pekeris approximation [13]. Solutions for the γ-unstable case and the exactly separable case with $\gamma \approx 0$ (to be called ES-M) have been obtained [14].

A few advantages of the present approach are listed here.

1) A well known problem of X(5) and related solutions is the overprediction of the energy spacings within the beta band by almost a factor of two [3]. It is known that this problem can be avoided by replacing the infinite-well potential of X(5) by a potential with sloped walls [15]. The present solution avoids this problem, since the right branch of the Morse potential imitates the sloped wall.

2) In X(5) and related models, using potentials of the form $u(\beta,\gamma) = u(\beta) + u(\gamma)$, the ground state and beta bands depend only on the parameters of the β potential, while the gamma bands depend also on an additional parameter introduced by the γ potential [usually the stiffnes of the harmonic oscillator used as $u(\gamma)$]. When exactly separable potentials of the form $u(\beta,\gamma) = u(\beta) + u(\gamma)/\beta^2$ are used, all bands (ground state, beta, gamma) depend on all parameters. Thus, all bands are treated on an equal footing, as in the case of the ES-D solution [16].

The original collective Bohr Hamiltonian is

$$H = -\frac{\hbar^2}{2B}\left[\frac{1}{\beta^4}\frac{\partial}{\partial\beta}\beta^4\frac{\partial}{\partial\beta} + \frac{1}{\beta^2\sin 3\gamma}\frac{\partial}{\partial\gamma}\sin 3\gamma\frac{\partial}{\partial\gamma}\right.$$

$$\left. -\frac{1}{4\beta^2}\sum_{k=1,2,3}\frac{Q_k^2}{\sin^2\left(\gamma-\frac{2}{3}\pi k\right)}\right] + V(\beta,\gamma), \qquad (1)$$

where β and γ are the usual collective coordinates which define the shape of the nuclear surface. Q_k (k=1, 2, 3) represents the angular momentum components in the intrinsic frame, and B is the mass parameter. Reduced energies and reduced potentials are defined as $\epsilon = 2BE/\hbar^2$, $v = 2BV/\hbar^2$ respectively [1].

We first examine the $\gamma \approx 0$ case. In the case of the exactly separable potentials $u(\beta,\gamma) = u(\beta) + u(\gamma)/\beta^2$ mentioned above, the wave functions take the form

$\psi(\beta,\gamma,\theta_j) = \xi_L(\beta)\Gamma_K(\gamma)D^L_{M,K}(\theta_j)$, where θ_j ($j = 1, 2, 3$) are the Euler angles, $D(\theta_j)$ represents Wigner functions of these angles, L stands for the eigenvalues of the angular momentum, while M and K are the eigenvalues of the projections of the angular momentum on the laboratory-fixed z-axis and the body-fixed z'-axis respectively. The Schrödinger equation is thus separated, as in Refs. [4, 7], into a "radial" part (depending on β) and a γ part.

In the case of the Morse potential, using the Pekeris approximation [13] and solving the β equation through AIM (the details are given in Ref. [14]), we obtain the energy eigenvalues

$$\epsilon_{n,L} = \frac{\mu c_0}{\beta_e^2} - \left[\frac{\gamma_1^2}{2\beta_e\gamma_2} - \left(n+\frac{1}{2}\right)\frac{\alpha}{\beta_e}\right]^2, \tag{2}$$

where

$$c_0 = 1 - \frac{3}{\alpha} + \frac{3}{\alpha^2}, \quad c_1 = \frac{4}{\alpha} - \frac{6}{\alpha^2}, \quad c_2 = -\frac{1}{\alpha} + \frac{3}{\alpha^2}, \quad \alpha = a\beta_e, \tag{3}$$

$$\gamma_1^2 = 2\beta_e^2 - \mu c_1, \qquad \gamma_2^2 = \beta_e^2 + \mu c_2, \qquad \mu = \frac{L(L+1)}{3} + 2 + \lambda. \tag{4}$$

λ in the last equation comes from the exact separation of variables and is determined from the γ equation. We use the same γ potential $u(\gamma) = (3c)^2\gamma^2$ as in the Davidson case [16], leading to

$$\lambda = \epsilon_\gamma - \frac{K^2}{3}, \qquad \epsilon_\gamma = (3C)(n_\gamma + 1), \qquad C = 2c. \tag{5}$$

We now turn our attention to γ-unstable solutions. In this case, the reduced potential is assumed to be γ independent, $v(\beta,\gamma) = u(\beta)$. Then the wavefunction takes the form [4] $\psi(\beta,\gamma,\theta_j) = R(\beta)\Phi(\gamma,\theta_j)$. The equation which includes the Euler angles and γ has been solved by Bès [17]. In this equation, the eigenvalues of the second-order Casimir operator of SO(5) occur, having the form $\Lambda = \tau(\tau+3)$, where τ is the seniority quantum number, characterizing the irreducible representations of SO(5) and taking the values $\tau = 0, 1, 2, 3, \ldots$ [18].

The values of the angular momentum L are given by the algorithm

$$\tau = 3\nu_\Delta + \lambda, \qquad \nu_\Delta = 0, 1, 2, \ldots \qquad L = \lambda, \lambda+1, \ldots, 2\lambda-2, 2\lambda \tag{6}$$

(with $2\lambda - 1$ missing), where ν_Δ is the missing quantum number in the reduction $SO(5) \supset SO(3)$ [18]. The ground state band levels are determined by $L = 2\tau$ and $n = 0$.

Using the Pekeris approximation [13] and AIM (see Ref. [14] for the details), we

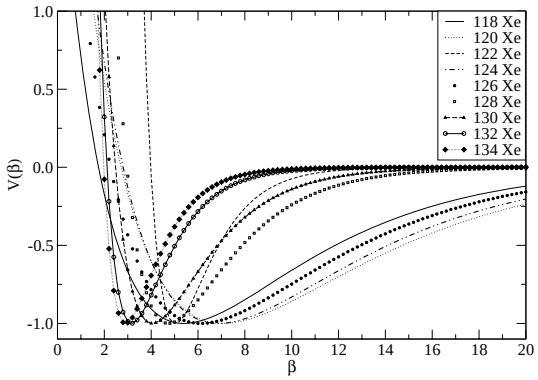

Fig. 1. Evolution of Morse potential shapes for the $_{54}$Xe isotopes, with the parameters given in Ref. [14].

obtain the energy eigenvalues

$$\epsilon_{n,\tau} = \frac{\nu c_0}{\beta_e^2} - \left[\frac{\gamma_1^2}{2\beta_e\gamma_2} - \left(n+\frac{1}{2}\right)\frac{\alpha}{\beta_e}\right]^2, \tag{7}$$

where

$$\gamma_1^2 = 2\beta_e^2 - \nu c_1, \qquad \gamma_2^2 = \beta_e^2 + \nu c_2, \qquad \nu = \tau(\tau+3)+2, \tag{8}$$

with the rest of the quantities given again by Eq. (3).

In order to test the applicability of the Morse potential in the description of nuclear spectra, we have fitted all nuclei with mass $A \geq 100$ and $R_{4/2} = E(4)/E(2) < 2.6$, for which at least the β_1 and γ_1 bandheads are known, using the γ-unstable solution of the Morse potential, which involves two free parameters (β_e, a). Results for 54 nuclei are shown in Ref. [14].

The Morse potentials obtained for the $_{54}$Xe isotopes are shown in Fig. 1. The evolution of the parameters and the shapes of the potentials are clear. As one moves from ^{134}Xe$_{80}$, which is just below the $N = 82$ magic number, to the mid-shell nucleus ^{120}Xe$_{66}$, the β_e parameter (which is the position of the minimum of the potential) increases, while the parameter a, which corresponds to the steepness of the potential, decreases. As a result, one gradually obtains less steep potentials with a minimum further away from the origin. The trends start to be reversed at ^{118}Xe$_{64}$, which is just below mid-shell.

We have also fitted all nuclei with mass $A \geq 150$ and $R_{4/2} = E(4)/E(2) > 2.9$ for which at least the β_1 and γ_1 bandheads are known, using the exactly separable rotational solution of the Morse potential with $\gamma \approx 0$ (ES-M), which involves three free parameters (the Morse parameters β_e and a, as well as the stiffness C of the γ potential). All bands are treated on an equal footing, depending on all three parameters. Results for 45 rare earths and 13 actinides are shown in Ref. [14].

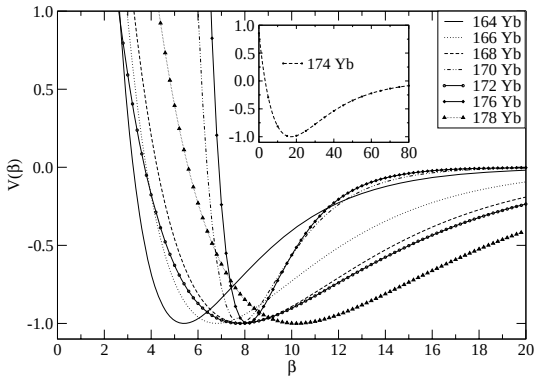

Fig. 2. Evolution of Morse potential shapes for the $_{70}$Yb isotopes, with the parameters given in Ref. [14].

The Morse potentials obtained for the $_{70}$Yb isotopes are shown in Fig. 2. The evolution of the parameters and the shapes of the potentials are again clear. As one moves from ^{164}Yb$_{94}$ to the mid-shell nucleus ^{174}Yb$_{104}$, the β_e parameter (which is the position of the minimum of the β-potential) again increases, while the parameter a, which corresponds to the steepness of the β-potential, again decreases. The C parameter, which is related to the stiffness of the γ-potential, increases. As a result, one gradually obtains less steep β-potentials with a minimum further away from the origin, while the γ-potentials get stiffer at the same time.

A notable exception occurs in the $N = 90$ isotones ^{150}Nd, ^{152}Sm, ^{154}Gd, which are known to be good examples of the X(5) critical point symmetry, along with ^{178}Os [3]. The relative failure of the Morse potential to describe critical nuclei is expected. The potential at the critical point is expected to be flat, as the infinite-well potential used in X(5), or to have a little bump in the middle [3]. Microscopic relativistic mean field calculations [19] of potential energy surfaces support these assumptions. Since the Morse potential cannot imitate a flat potential, with or without a bump in the middle, it is expected that it cannot describe these nuclei satisfactorily.

A comparison of the present fits (reported in Ref. [14]) to the results provided by the Davidson potential in the exactly separable $\gamma \approx 0$ case [16] (ES-D), which contains two free parameters (β_0, c) instead of three (see Table 1 of Ref. [16]), shows that the extra parameter extends the region of applicability of the model in most nuclei to higher angular momenta, largely improving the quality of the fits.

In summary, the Bohr Hamiltonian has been solved with the Morse potential for any angular momentum, both in the γ-unstable case and in the exactly separable rotational case with $\gamma \approx 0$ (in which a harmonic oscillator is used for the γ potential), labelled as ES-M. The solution has been achieved [14] through the Asymptotic Iteration Method (AIM) and has involved the Pekeris approximation.

Numerical results have been presented for both solutions, including all relevant

medium mass and heavy nuclei for which at least the β_1 and γ_1 bandheads are known. The success of the present solutions in reproducing quite well both the bandeahds of and the spacings within the ground, β_1 and γ_1 bands indicate that a detailed study of γ_2 and other higher bands within this framework might be fruitful. The influence of the finite depth of the potential is also worth considering in further detail. From the findings of Ref. [20], where the E(5) case was solved for a finite well, the influence of the finite depth of the potential is expected to show up more clearly in the higher excited states. Work on the calculation of wave functions and $B(E2)$ transition rates is in progress.

References

[1] F. Iachello, Phys. Rev. Lett. **85**, 3580 (2000).

[2] F. Iachello, Phys. Rev. Lett. **87**, 052502 (2001).

[3] R. F. Casten and E. A. McCutchan, J. Phys. G: Nucl. Part. Phys. **34**, R285 (2007).

[4] L. Wilets and M. Jean, Phys. Rev. **102**, 788 (1956).

[5] J. Meyer-ter-Vehn, Nucl. Phys. **A 249**, 111 (1975).

[6] D. Bonatsos, D. Lenis, D. Petrellis, and P. A. Terziev, Phys. Lett. **B 588**, 172 (2004).

[7] L. Fortunato, Eur. Phys. J. A **26**, s01, 1 (2005).

[8] D. Bonatsos, D. Lenis, and D. Petrellis, Romanian Reports in Physics **59**, 273 (2007). ArVix nucl-th/0701055.

[9] S. Flügge, *Practical Quantum Mechanics* (Springer, Berlin, 1974).

[10] F. Cooper, A. Khare, and U. Sukhatme, *Supersymmetry in Quantum Mechanics* (World Scientific, Singapore, 2001).

[11] H. Ciftci, R. L. Hall and N. Saad, J. Phys. A: Math. Gen. **36**, 11807 (2003).

[12] H. Ciftci, R. L. Hall and N. Saad, J. Phys. A: Math. Gen. **38**, 1147 (2005).

[13] C. L. Pekeris, Phys. Rev. **45**, 98 (1934).

[14] I. Boztosun, D. Bonatsos, and I. Inci, Phys. Rev. C **77**, 044302 (2008).

[15] M. A. Caprio, Phys. Rev. **C 69**, 044307 (2004).

[16] D. Bonatsos, E. A. McCutchan, N. Minkov, R. F. Casten, P. Yotov, D. Lenis, D. Petrellis, and I. Yigitoglu, Phys. Rev. C **76**, 064312 (2007).

[17] D. R. Bès, Nucl. Phys. **10**, 373 (1959).

[18] G. Rakavy, Nucl. Phys. **4**, 289 (1957).

[19] R. Fossion, D. Bonatsos, and G. A. Lalazissis, Phys. Rev. C **73**, 044310 (2006).

[20] M. A. Caprio, Phys. Rev. **C 65**, 031304 (2002).

'Study of the d+^{11}B system differential cross sections for NRA purposes'

M. Diakaki[(1)], M. Kokkoris[(1)], P. Misaelides[(2)], X. Aslanoglou[(3)], A. Lagogiannis[(4)], C. Raepsaet[(5)], V. Foteinou[(1)], S. Harissopulos[(4)], R. Vlastou[(1)], C.T. Papadopoulos[(1)]

[(1)]Department of Physics, National Technical University of Athens, Zografou campus, Athens 15780, Greece
[(2)]Department of Chemistry, Aristotle University of Thessaloniki, Thessaloniki 54124, Greece
[(3)]Department of Physics, University of Ioannina, Ioannina 45110, Greece
[(4)]Institute of Nuclear Physics, TANDEM Accelerator, N.C.S.R. 'Demokritos', Aghia Paraskevi, Athens 15310,Greece
[(5)]Laboratoire Pierre-Sue, CEA-CNRS UMR-9956, CEA Saclay, 91191, Gif-Sur-Yvette, France

The accurate quantitative determination and depth profiling of the element boron is nowadays of extreme importance in many technological applications (semiconductor technology, plasma technology etc) and environmental research activities. However, as boron is usually present in heavy matrices along with other light elements its determination has been a challenge for all Ion Beam Analysis (IBA) techniques.
Nuclear Reaction Analysis (NRA) is well established nowadays as one of the principal IBA techniques, due to its advantages: high isotopic selectivity and capability of least destructive depth profiling. Specially when deuterium is the probing beam (d-NRA) critical advantages emerge, such as a) the possibility for simultaneous activation, and thus analysis, of all the light elements that usually coexist in samples (e.g. C, O, B, N etc), b) the enhanced sensitivity and accuracy (due to the large cross sections of the deuteron induced reactions), c) the low beam energy required and d) the low energy loss in the material, compared to the ^{3,4}He. In order for d-NRA to be used in the determination of boron, the absolute values of the cross sections of the reactions of the deuterium with boron are necessary. These values cannot be theoretically predicted for light nuclei, such as boron, and have to be determined experimentally. However a lack of such experimental data has been pointed out for the d+^{11}B system, despite the fact that ^{11}B is the main constituent isotope of natural boron (80%) and the high Q-value of the reaction ^{11}B(d,α_0) (8031.2 keV).
Therefore, the present work aims to contribute to the field of boron profiling, through the determination of the absolute differential cross sections of the reactions ^{11}B(d,p) and ^{11}B(d,α), using a deuteron beam of energy 900-1200keV in the lab system (step: 25keV), at detection angles 140^o-170^o (step:10^o). The experiment took place at the I.N.P.R of the N.C.S.R 'Demokritos', by using the 5.5 MV TN11 Van de Graaff TanDem accelerator. The values of the differential cross sections are validated through a benchmarking experiment, using a high purity thick B_4C target, and are already available to the scientific community for application through IBANDL (www-nds.iaea.org/ibandl/). The experimental procedure, the data analysis and the results, as well as the comparison of d-NRA with other techniques (including IBA) in the determination of boron were presented and discussed, and more details can be found in the published paper: M. Kokkoris, M. Diakaki, P. Misaelides, X. Aslanoglou, A. Lagoyannis, C. Raepsaet, V. Foteinou, S. Harissopulos, R. Vlastou, C.T. Papadopoulos, *Nuclear Instruments and Methods in Physics Research B* ***267*** *(2009) 1740–1743.*

A CBF calculation of $^1S_0$ Superfluidity in the Inner Crust of Neutron Stars

G. Pavlou[a], E. Mavrommatis[a], Ch. Moustakidis[b], J. W. Clark[c]

[a] *Physics Department, Division of Nuclear and Particle Physics, University of Athens, GR – 15771 Athens, Greece*
[b] *Department of Theoretical Physics, Aristotelian University of Thessaloniki, GR – 54124 Thessaloniki, Greece*
[c] *McDonnell Center for the Space Sciences and Department of Physics, Washington University, St. Louis, MO 63130, USA*

Abstract

Singlet S-wave superfluidity of dilute neutron matter in the inner crust of neutron stars is studied within the correlated BCS (Bardeen, Cooper, Schrieffer) method, taking into account both pairing and short-range correlations. First, the equation of state (EOS) of normal neutron matter is calculated within the correlated-basis-function (CBF) method in lowest cluster order using the Argonne V_{18} and $V_{4'}$ potentials and Jastrow-type correlation functions. The $^1S_0$ superfluid gap is then calculated with these potentials and correlation functions. The dependence of our results on the choice of the correlation functions is analyzed and the role of higher-order cluster corrections is considered. The values obtained for the $^1S_0$ gap within this simplified scheme are comparable to those from other, more elaborate, methods.

1. Introduction

The matter in the inner crust matter of neutron stars consists of dilute neutron fluid (with $0.2\ \mathrm{fm}^{-1} \lesssim k_F \lesssim 1.3\ \mathrm{fm}^{-1}$, where k_F is the Fermi wavenumber) interpenetrating a lattice of neutron-rich nuclei that dissolves in the interface with the quantum fluid interior. The neutron system is expected to be in a superfluid phase associated with pairing in the $^1S_0$ channel. The existence of such a phase has direct consequences for post-glitch relaxation and other observed phenomena [1]. The $^1S_0$ superfluid gap has been calculated using various methods of many-body theory. Due to the differences of theoretical methods and assumptions made for the pairing interaction and single-particle energies, there remains considerable ambiguity in the value of the gap as a function of k_F or the density ρ. In this paper we apply the method of CBF in lowest order and evaluate the EOS of normal dilute neutron matter using the Argonne V_{18}

Email address: gepavlou@phys.uoa.gr (G. Pavlou)

and the simpler $V_{4'}$ potentials. The $^1S_0$ superfluid gap is then determined by implementing a generalization of the BCS theory within the CBF framework. The calculational strategy is described in Section 2. As discussed in Section 3, the results are found to be comparable to those reported by other authors. Among other aspects of the problem, we investigate the sensitivity of the calculated quantities to the type of short-range correlations assumed and to the contribution of P waves. Further details will be reported in a longer article [2].

2. Calculational Methods

2.1. Equation of State

In calculating the EOS of dilute neutron matter we apply the CBF method [3], in which a correlation operator $F(1,...,N)$ is used to generate a complete set of non-orthogonal correlated wave functions in the N-particle Hilbert space:

$$|m\rangle \equiv |\Psi_m\rangle = I_{mm}^{-1/2} F(1,...,N)|\Phi_m\rangle. \tag{1}$$

$|\Phi_m\rangle$ is an appropriate basis of independent-particle wavefunctions and I_{mm} is a normalization constant. For normal neutron matter, the $|\Phi_m\rangle$ are chosen as Slater determinants of plane waves. The Hamiltonian matrix elements are calculated by using the above non-orthogonal correlated basis with perturbation expansion and cluster approximations. Well-known steps [3] lead to the following variational expression for the energy per neutron (equivalent to first-order perturbation theory in the correlated basis):

$$\frac{E}{N} = \frac{3}{5}E_F + 2\pi\rho \sum_{spin} \int_0^\infty w_2^{spin}(r) G_{spin}(k_F r) r^2 dr. \tag{2}$$

E_F is the ideal Fermi gas energy, $w_2^s(r) = \frac{\hbar^2}{m}\left(\vec{\nabla} f_s(r)\right)^2 + \upsilon_s(r) f_s^2(r)$ are the components of the spin-dependent effective two-neutron interaction in an operatorial decomposition ($s = 1, 2$), the functions $\upsilon_s(r)$ are the corresponding components of the bare spin-dependent two-neutron interaction itself, $f_s(r)$ is a Jastrow two-body correlation function and the quantities G_s are the spin-dependent radial distribution functions. The numerical calculations of E/N are carried out for the Argonne V_{18} [4] potential and the simpler $V_{4'}$ model [5]. Two parametrized correlation functions were studied, (i) the so-called Davé form [6] $f_s(r) = \exp\left\{-\frac{1}{2}\left(\frac{b}{r}\right)^m \exp\left[-\left(\frac{r}{b}\right)^n\right]\right\}$ with parameters b, m and n and (ii) the Benhar form $f_s(r) = [1-\exp(-(r^2/b^2)]^2 + gr\exp(-r^2/c^2)$, with parameters b, c while g is determined by an orthogonality condition for each spin state. In the first set of calculations, we include only contributions from the $S = 0$, $L = 0$ state ("singlet-S only"); in the second, we also include contributions from $S = 1$, $L = 1$ (triplet-P states). The same two functional forms of $f_s(r)$ are considered for the pure $^1S_0$ case and the case including ^3P-state contributions but somewhat different parameter sets are produced when the variational principle is applied.

2.2. $^1S_0$ *Superfluid Gap*

A generalization of BCS theory within the CBF framework [8] is employed to study superfluidity in the dilute neutron-matter system. The dynamically correlated superfluid state is given formally by

$$|CBCS\rangle = \sum_N \sum_m \left(I_{mm}^{(N)}\right)^{-1/2} F_N \left|\Phi_m^{(N)}\right\rangle \left\langle \Phi_m^{(N)} \;\middle|\; BCS \right\rangle \tag{3}$$

where the kets $|\Phi_m^{(N)}\rangle$ are Slater determinants defined for occupied Fermi sea orbitals, $m = m_1, \ldots, m_N$, while $|BCS\rangle$ is the BCS state. Given Eq. (3), steps similar to those of BCS theory, involving evaluation of the expectation value of $\hat{H} - \mu\hat{N}$ in the state (3), where μ is the chemical potential and $\hat{N}$ the number operator, and application of the variational principle, lead [8] ultimately to the familiar gap equation

$$\Delta(k) = -\frac{1}{\pi} \int_0^\infty \frac{V(k,k')}{\sqrt{\left(\varepsilon(k') - \mu\right)^2 + \Delta^2(k')}} \Delta(k') k'^2 dk' \tag{4}$$

but with the bare pairing interaction replaced by its correlation-renormalized version $V_{kk'} = kk'^{-1} \int_0^\infty w_2^{^1S_0}(r) \sin(kr) \sin(k'r) dr$ and the single-particle energies $\varepsilon(k')$ by their CBF counterparts. The same dynamical correlation function $f_s(r)$ is used for both superfluid and normal states. Equation (4) is a singular, nonlinear integral equation. Straightforward solution by an iterative method is possible, if one takes a starting value of the gap from Ref. [6]. A more robust and efficient iteration procedure is based on the separation method [9], in which Equation (4) is first transformed into a system of two coupled equations, namely a "quasi-linear" integral equation for the shape of $\Delta(k)$ and an algebraic equation for its amplitude.

3. Results and Discussion

3.1. Equation of State

In Figure 1 we plot the energy per neutron as a function of k_F for the V_{18} potential and selected dynamical correlation functions. For a given potential, differences (generally small) are seen in the results for the different correlation functions. This is expected since, in particular, the Benhar correlation function overshoots unity whereas the Dáve function does not. Moreover, if we compare E/N results for the singlet-S-only case with those when the P-wave contribution is included, this positive contribution is seen to increase with density and begins to play an important role. Inclusion of the P-wave contribution is necessary for $k_F \gtrsim 0.8 fm^{-1}$. We remark further that the results obtained with (V_{18} and $V_{4'}$) are similar for the same type of correlation function. This implies that in the density range considered, the additional complications present in the highly realistic V_{18} interaction are of little importance. We also infer that the higher-order

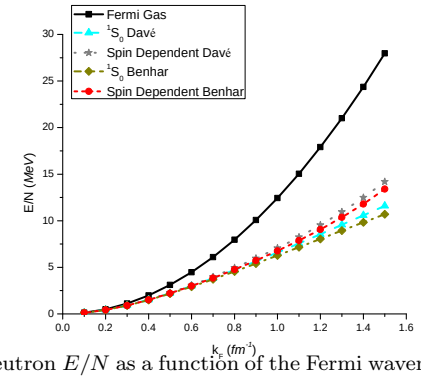

Figure 1: Energy per neutron E/N as a function of the Fermi wavenumber k_F for the potential V_{18} for various cases (see text). We also plot the ideal Fermi gas energy per neutron for comparison.

cluster terms omitted are not essential in this density range, based on the relatively small values of the "wound parameter" $\xi = \rho|\int d^3r[f^2(r)-1]|$ associated with the optimized two-body correlations. Our results for E/N may be compared with those from other methods, including relativistic mean-field methods [10], the variational method [11], the Bethe-Brueckner-Goldstone (BBG) theory [12], and Monte Carlo methods (Green Function Monte Carlo [13] (GFMC) and Auxiliary Field Diffusion Monte Carlo [14] (AFDMC)). Our calculations show reasonably good agreement with these results, the best agreement being achieved when the Benhar correlation function is used and P-wave contributions are included. The main reason that such a simple method is adequate stems from the fact that at the neutron densities of the inner crust of a neutron star, one does not see the large-scale cancellations between kinetic and potential contributions to E/N that make precise calculations more difficult at nuclear density and higher, especially in symmetrical nuclear matter. Finally, three-nucleon interactions are not expected to be important at these densities.

3.2. $^1S_0$ *Superfluid Gap*

We solve the gap equation (4) using the separation method [9], adopting the correlation functions that were determined for the normal state. The resulting energy gap on the Fermi surface, $\Delta(k_F) = \Delta_F$, is plotted in Figure 2 as a function of k_F for the case of the V_{18} interaction (we have also solved the gap equation by straightforward iteration, taking properly into account the small values of the denominator on the Fermi surface with similar results). Similar calculations have been performed for the $V_{4'}$. The density range over which a nonzero gap is found using Davé correlations is larger than that for Benhar correlations. The gap range we found using the Davé type correlations are larger than the ones with Benhar type correlations. Upon comparing the values for the gap Δ_F in the singlet-S-only case with those found including the P-wave contribution to E/N, it is seen that the latter are slightly smaller than the former. Thus, inclusion of the P channel has a small negative effect on

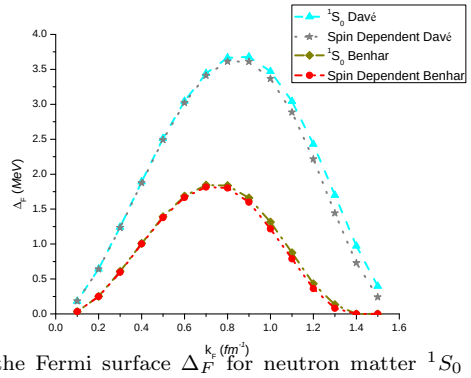

Figure 2: The gap in the Fermi surface Δ_F for neutron matter $^1S_0$ superfluid state as a function of the Fermi wavenumber k_F with the V_{18} potential for various cases (see text).

the gap. This is true for either form of the correlation function. Moreover, when comparing the gap results for the $V_{4'}$ potential with those for the V_{18}, we observe that the former are only slightly different, which is consistent with the expectation that higher-order partial waves have little influence on the value of the $^1S_0$ gap. Comparing our results with those from the simple BCS method with a bare pairing interaction [9] and no corrections for geometrical correlations or polarization effects, we find that our results based on Benhar correlations are somewhat smaller. As previously mentioned, gap calculations have been performed by a number of other methods, including the non-orthogonal CBF approach [6, 15], the orthogonal CBF scheme [16], the renormalization-group technique [17], BBG theory [18], GFMC [13], AFDMC [14], and more [19, 20, 21]. Some of the results are displayed in Figure 3. All of the calculations so represented give results for the gap lower than the pure BCS treatment with a bare pairing interaction. Our results for Benhar correlations are closest to those of Refs. [13, 18, 21]; in addition, the density at which the gap reaches a maximum is similar to the values found in Refs. [15, 18, 19, 21]. In these two respects, the Benhar choice of correlation function is the more realistic for the study of neutron matter in the supefluid state. It is not surprising that there still remains considerable uncertainty in quantitative determination of the behavior of the $^1S_0$ gap Δ_F, in view of the exponential sensitivity of this quantity to the inputs for pairing interaction and density of states.

References

[1] P. Haensel, A.Y. Potekhin, and D.G. Yakovlev, *Neutron Stars 1, Equation of State and Structure*, Springer (2007).

[2] G. Pavlou, Master Thesis, University of Athens; G. Pavlou, E. Mavrommatis, Ch. Moustakidis, J. W. Clark, to be published.

[3] J. W. Clark et al., Nucl. Phys. A328 (1979) 45.

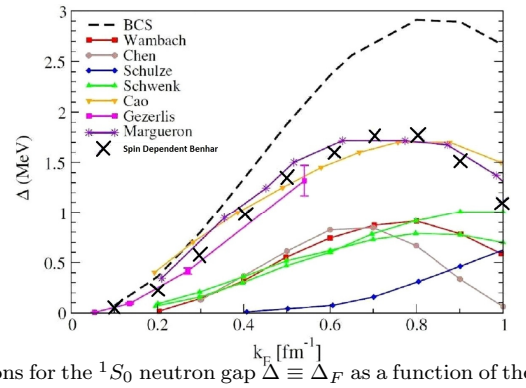

Figure 3: Calculations for the $^1S_0$ neutron gap $\Delta \equiv \Delta_F$ as a function of the Fermi wavenumber k_F with various methods (see text) : BCS [9], Wambach [19], Chen [15], Schulze [20], Schwenk [17], Cao [18], Gezerlis [13], Margueron [21], as seen in Ref.[14], and, with Black X, our results with Benhar type correlation function in the spin-dependent case using the V_{18} potential.

[4] R. B. Wiringa, V. G. Stoks, and R. Schiavilla, Phys. Rev. C51 (1995) 38.

[5] R. B. Wiringa and S. C. Pieper, Phys. Rev. Lett. 89 (2002) 182501.

[6] J. M. C. Chen et al., Nucl. Phys. A555 (1993) 59.

[7] O. Benhar et al., Phys. Lett. B60 (1976) 129.

[8] E. Krotscheck and J. W. Clark, Nucl. Phys. A333 (1980) 77; E. Krotscheck, R. A. Smith, and A. D. Jackson, Phys. Rev. B24 (1981) 6404.

[9] V. A. Khodel, V. V. Khodel, J. W. Clark, Nucl. Phys. A598 (1996) 390.

[10] J. Piekarewicz, Phys. Rev. C76 (2007) 064310.

[11] B. Friedman and V. R. Pandharipande, Nucl. Phys. A361 (1981) 501.

[12] M. Baldo and C. Maieron, Phys. Rev. C77 (2008) 015801.

[13] A. Gezerlis and J. Carlson, Phys. Rev. C77 (2008) 032801.

[14] S. Gandolfi et al., Phys. Rev. Lett. 101 (2008) 132501; Phys. Rev. C79 (2009) 054005.

[15] J. M. C. Chen et al., Nucl. Phys. A451 (1986) 509.

[16] A. Fabrocini et al., Nucl. Phys. A803 (2008) 137.

[17] A. Schwenk, B. Friman, and G. E. Brown, Nucl. Phys. A713 (2003) 191.

[18] L. G. Cao, U. Lombardo, and P. Schuck, Phys. Rev. C74 (2006) 064301.

[19] J. Wambach, T.L. Ainsworth, and D. Pines, Nucl. Phys. A555 (1993) 128.

[20] H.-J. Schulze et al., Phys. Lett. B375 (1996) 1.

[21] J. Margueron, H. Sagawa, and K. Hagino, Phys. Rev. C76 (2007) 064316.

Monte Carlo simulation of a NaI detector in the aquatic environment

C. Bagatelas[a, b*], C. Tsabaris[a], M. Kokkoris[b], C.T. Papadopoulos[b], R. Vlastou[b]

[a]*Hellenic Centre for Marine Research, Institute of Oceanography, 19013 Anavyssos, Greece*

[b]*National Technical University of Athens, Dep. of Applied Mathematics and Physics, 15780 Zografou, Greece*

Abstract

NaI(Tl) crystals are used in many marine applications for continuous measurements with buoy operation and autonomous in situ measurements in seawater. Monte Carlo simulations were performed using the GEANT4 code for the investigation of the γ-ray absorption in water in different spherical geometries and for the efficiency of a NaI(Tl) detector of different radionuclides in the aquatic environment. In order to test the reliability of these simulations, experimental values of the NaI(Tl) detector efficiency were deduced using a special tank filled with water and reference single gamma ray sources (^{99m}Tc, ^{137}Cs and ^{40}K). The cascade reference source ^{111}In was also diluted in tank for comparison with the reproduction spectra of its cascade lines as provided with the GEANT4 code. The results are in good agreement with the simulated ones within uncertainties.

Keywords: Monte Carlo simulation; GEANT4 code; marine efficiency

1. Introduction

The quantitative measurements of radioactivity in the aquatic environment is a complicated task since it demands robust underwater system, stable electronics, optimum housing material, precise calibrations. *In situ* detection systems for long-term aquatic measurements are very scarce due to the power consumption limitation of the systems and to the high background originating from Compton scattering of 1461 keV (^{40}K) and 2615 keV (^{208}Tl) γ-rays. NaI(Tl) are the most common crystals for long term measurements due to their low consumption, good efficiency and low cost [1], but they have the disadvantage of low energy resolution. Such crystals are contemporarily used in many oceanographic applications, using continuous measurements for radiation monitoring with buoy operation and *in situ* measurements in seawater [2-6]. A lot of effort has been made during the last years for the experimental calibration of detection systems in water tanks, by diluting calibrated standard sources [7-9].

The detection efficiency for aquatic environments can not be determined for all γ-ray energies experimentally, but only using specific gamma ray reference sources and simulation codes. In order to determine the efficiency for each γ-ray energy, in the present work, a Monte Carlo simulation was performed using the GEANT4 code for studying the photon interaction in water in different spherical geometries and for calculating the detection efficiency for different radionuclides in the marine environment.

* Corresponding author.
Tel.: +3022910 76410; *Fax*: +3022910 76323; *E-mail address*: cbagatelas@gmail.com (C. Bagatelas).

In an attempt to increase the confidence of the spectra analysis and produce more reliable results in the concentration of low-level environmental radioactivity, simulated spectra of ^{99m}Tc, ^{137}Cs and ^{111}In were compared with real data recorded by the detector in a water tank. In addition the comparison between the measured spectra and the simulated ones could control any possible performance deterioration of the submersible detection system at an early stage.

2. Description of the experimental and simulated setup

2.1. System Description

For the in situ monitoring of radioactivity in the marine environment a new 7.5×7.5 cm NaI(Tl) scintillator detector coupled with a photomultiplier and integrated electronics, was developed at the Hellenic Centre for Marine Research. It is an autonomous system with relatively low power consumption, operational on oceanographic buoys and seabed platforms. The design and special characteristics of the developed system are described elsewhere [9]. The detection system had to be tested and calibrated in the laboratory, in a water tank, before its deployment in the marine environment. The layouts of the water tank, along with the schematic geometry of the detector are shown in Figure 1.

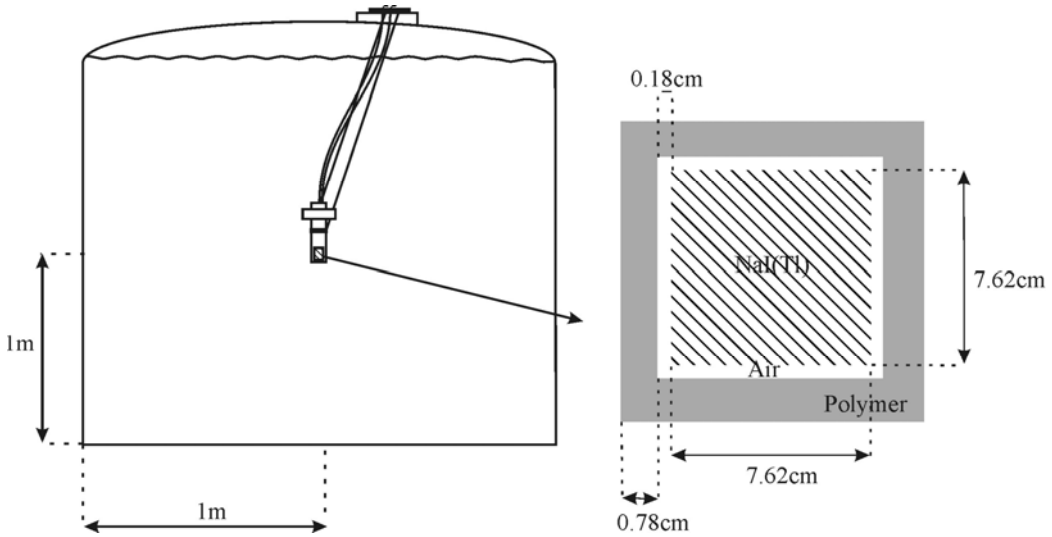

Fig. 1. Layout of the water tank along with the NaI(Tl) detector geometry, used both for the simulations and experimental calibration [11].

2.2. Simulation code description

GEANT4 is a Monte Carlo code, which simulates the trajectory of elementary particles through matter. It simulates the tracking of particles, like γ-rays, through an experimental setup for the study of the detector response. It also provides the graphical representation of the setup and of the particle trajectories [10]. Detailed descriptions of the geometry of the experimental setup with respect to their dimensions, materials and shapes, as well as, of the particle generator, are required by the program to simulate and store the history of each particle from its generation to full deposition of its energy in the detector. The definition of the parameters, which control the Monte Carlo simulation, is of particular importance for the quality of the results. The specific details and characteristics of the code as implemented in a NaI(Tl) system have been extensively described in the past [11].

3. The GEANT4 code simulations

The detection system is designated to measure γ-ray radioactivity in the marine environment. The aim of this work is to accurately convert the photopeak counts corresponding to each radionuclide in the recorded spectrum, to specific activity in Bq/m^3. The specific activity, r, is given by the Equation (1):

$$r(Bq/m^3) = \frac{CPS}{\varepsilon \cdot V \cdot I_\gamma} \quad (1)$$

Where CPS denotes counts per second recorded for the specific radionuclide, ε is the photopeak efficiency at the specific energy, V the volume of water for each γ-ray and I_γ is the emission probability of the specific γ-ray. In order to use Eq. (1) in a global, consistent and reliable way in the case of marine measurements, the product (ε·V), which subsequently is denoted as "marine efficiency" ε_m (in m^3), has to be defined for all γ-ray energies.

The corresponding spherical volume, V_{eff}, surrounding the detector, beyond which γ-rays have practically zero probability to reach and interact with the detector crystal will be defined as the "effective volume" for the specific γ-ray energy.

3.1. Marine efficiency

The calculation of the NaI(Tl) detector efficiency for each γ-ray energy depends strongly on the volume of water mass. Gamma rays of different energies present different absorption in water so that the detector efficiency varies for different effective water volumes. In an attempt to quantitatively study this effect, simulations have been carried out via the GEANT4 code for different radionuclides diluted in different water volumes surrounding the NaI(Tl) detector. As input, three γ-rays, namely 140.5 (^{99m}Tc), 661.6 (^{137}Cs) and 1460.6 keV (^{40}K) were used to produce simulated spectra via the GEANT4 code for various spherical water volumes. For each water volume, the density of counts (counts/m^3) was kept constant, so that the variation of photopeak counts could be studied as a function of water volume. It was observed that the photopeak counts are increasing with volume and exhibit a saturated value for water volumes greater than the effective one. In the case of ^{137}Cs (661.6 keV) the results are shown in Figure 2 along with the fitting curve. The marine efficiency, ε_m, was deduced by dividing the saturated counts with the total number of counts in each spectrum and by multiplying with the respective volume. It was thus also observed that the marine efficiency remains constant for volumes larger than the effective volume.

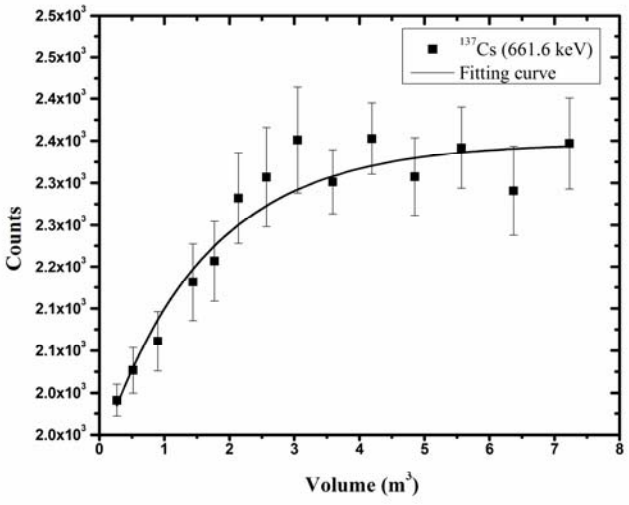

Fig. 2. Graphic representation of detected counts in the 661 keV photopeak of the simulated spectrum, associated to the volume of water with diluted ^{137}Cs. The solid line represents an exponential fitting curve of the simulated values.

In order to calculate the marine efficiency, ε_m, of the NaI(Tl) detector in the aquatic environment as a function of energy, simulated spectra were generated for the energy range between 100 and 2000 keV. The results are shown in Figure 3 and the error bars in the figure correspond to the statistics of the simulated spectra. The solid line represents the marine efficiency curve, which fits the simulated values in water and is given by the empirical expression [12]:

$$\varepsilon_m = \frac{a \cdot E^b}{c + E^d} \tag{2}$$

Where α, b, c and d are fitted parameters and E is the energy of the specific γ-ray.

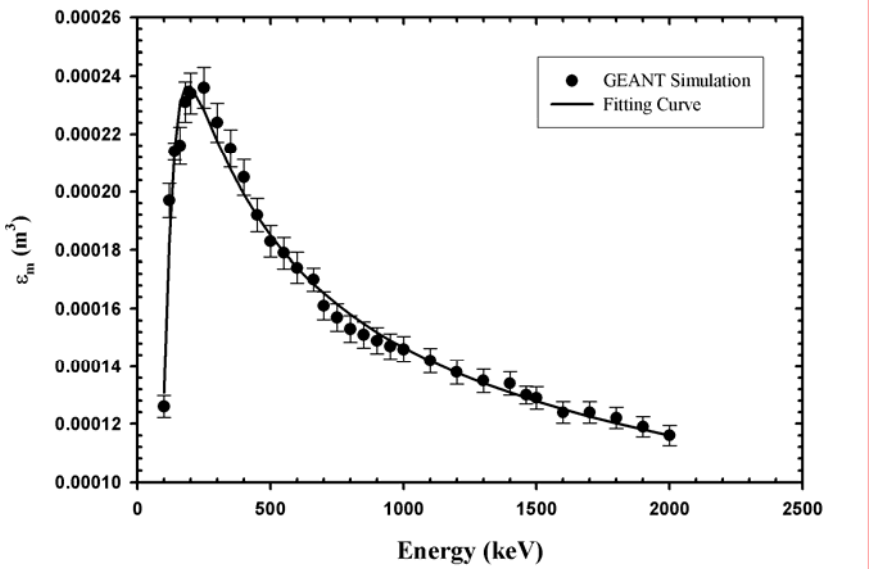

Fig. 3. Simulated marine efficiency values of the NaI(Tl) detector in the aquatic environment along with the fitting curve (solid line) from Eq. (2).

Experimental values [9] of the NaI(Tl) detector marine efficiency, ε_m, (extracted for the 140.5, 661.6 and 1460.6 keV transitions of ^{99m}Tc, ^{137}Cs and ^{40}K, respectively) were deduced and seem to be in good agreement with the simulated ones. The experimental and simulated marine efficiency values seem to agree within the 10% uncertainty values. These results indicate that the marine efficiency of the NaI(Tl) spectrometer as simulated by the GEANT4 code, could be used over the full energy range for the determination of the volumetric activity of radionuclides emitting non cascade γ-rays in water.

3.2. Experimental and simulated spectra

In the present work simulated spectra of ^{99m}Tc (140.5 keV), ^{137}Cs (661.6 keV) and ^{111}In (172 keV and 246 keV) were reproduced and compared with the equivalents experimental that were recorded by the detector in a water tank. More specifically, the sensor was mounted in the middle of the water tank, of 5.5 m^3 volume and appropriate radionuclides (^{99m}Tc, ^{137}Cs and ^{111}In) were diluted. The recorded spectra (after the subtraction of the corresponding background spectrum) were used for the comparison with the simulated ones. A rebinning algorithm has been applied to the experimental spectra before the fitting procedure. In following figures (Fig. 4a-c) the experimental spectra are shown, along with the simulated ones.

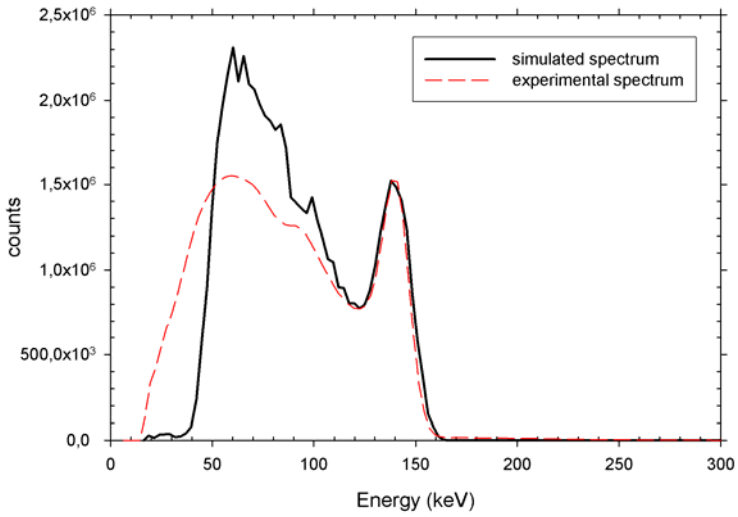

(a)

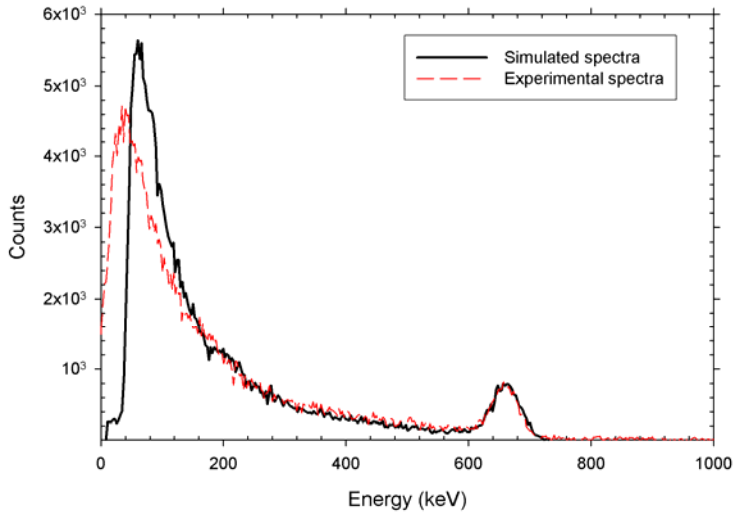

(b)

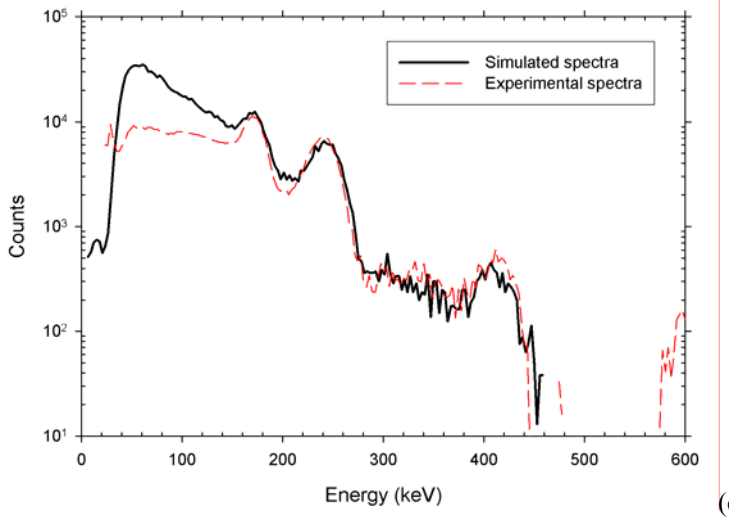

(c)

Fig. 4. Simulated and real spectra, acquired by the NaI(Tl) detector in a water tank with diluted (a) ^{99m}Tc, (b) ^{137}Cs and (c) ^{111}In (the background spectrum has been subtracted from the experimental spectra).

4. Discussion of the results

The GEANT4 code successfully describes the detection process for qualitative, as well as, quantitative marine radioactivity calculation using the NaI(Tl) detection system and produces reliable γ-ray spectra of natural radionuclides collected by a NaI(Tl) detector immersed in an aquatic environment. The simulated spectra can be used to calculate the marine efficiency, ε_m, in a wide energy range and thus to determine the volumetric activity in Bq/m^3 for γ-emitter radionuclides.

It must be emphasized that the calibration factors for the marine efficiency are valid only in the case of single energy γ-emitting radionuclides. In the case of cascade energy γ-emitting radionuclides the results are not appropriate since summing effects should also be taken into account.

The simulated spectra for ^{99m}Tc, ^{137}Cs and ^{111}In agree well with the experimental ones except in the lowest energy region. More specifically, above 180 keV simulated and experimental spectra coincide, but in the low-energy region (<180 keV) the simulation overestimates the experimental spectra. In the case of cascade reference source ^{111}In the simulated and experimental spectrum are in good agreement. So the simulation code reproduces with grate accuracy summing effects from cascade energy γ-emitting radionuclides.

5. Conclusions

A method for improving the accuracy of the determination of radioactivity in the marine environment has been developed, aiming at its integration on geophysical applications, as well as, at real-time data-forwarding buoy applications. The marine efficiency of a NaI(Tl) detector was investigated experimentally and with computer simulations using the GEANT4 code. It was proven that the code provides quantitatively accurate results and is suitable for marine applications. Thus, the simulations constitute a useful tool, especially in the case where the experimental setup for the detector calibration cannot effectively imitate the marine environment, for the investigation of problems of γ-ray absorption in water and solid angle calculations that are present for *in situ* marine measurements.

References

[1] P.P. Povinec, I. Osvath, M.S. Baxter, Applied Radiation Isotopes 47 (1996) 1127-1133.
[2] U.R. Aakenes, Chemistry and Ecology 10 (1995) 61-69.
[3] T.H. Soukissian, G.T. Chronis, K. Nittis, Sea Technology 40 (1999) 31-37.
[4] Ch. Wedekind, G. Schilling, M. Grüttmüller, K. Becker, Applied Radiation and Isotopes 50 (1999) 733-741.
[5] C. Tsabaris, D. Ballas, Applied Radiation and Isotopes 62 (2005) 83-89..
[6] I. Osvath, P.P. Povinec, H.D. Livingston, T.P. Ryan, S. Muslow, J.-F. Commanducci, Journal of Radioanalytical and Nuclear Chemistry 263 (2005) 437-440.
[7] P. Vojtyla, Applied Radiation and Isotopes 55 (2001) 81-88.
[8] P. van Put, A. Debauche, C. De Lellis, V. Adam, Journal of Environmental Radioactivity 72 (2004) 177-186.
[9] C. Tsabaris, C. Bagatelas, Th. Dakladas, C.T. Papadopoulos, R. Vlastou, G.T. Chronis, Applied Radiation and Isotopes 66 (2008) 1419-1426.
[10] CERN, GEANT Detector Description and Simulation Tool. CERN Program Library Office, CERN, Geneva, 1993.
[11] R. Vlastou, I.Th. Ntziou, M. Kokkoris, C.T. Papadopoulos, C. Tsabaris, Applied Radiation and Isotopes 64 (2006) 116-123.
[12] K. Debertin, R.G. Helmer, Gamma- and X-ray Spectrometry with Semiconductor Detectors, North-Holland, Amsterdam, 1988.

Vertical distribution of ^{137}Cs and natural radioactivity in core sediments of Thermaikos Gulf, northwestern Aegean Sea

G. Eleftheriou[a,b*], C. Tsabaris[a], E. Philis-Tsirakis[b], E. Kaberi[a], R. Vlastou[b]

[a]*Hellenic Centre for Marine Research, Institute of Oceanography, 19013 Anavyssos, Greece*

[b]*National Technical University of Athens, Dep. of Applied Mathematics and Physics, 15780 Zografou, Greece*

Abstract

Sub-superficial sediments have been collected from the Thermaikos Gulf, located in the NW Aegean Sea, in order to determine sedimentation rates using vertical distributions of ^{137}Cs and ^{210}Pb. In addition measurements of the characteristic radionuclides of the ^{238}U and ^{232}Th natural series has also been performed to better understand the transport and the sedimentation process in a marine environment, which is strongly influenced by the main North Greece rivers. The sedimentation rates of the five selected cores using the two methods were consistent and varied from 0.20 ± 0.01 till 0.30 ± 0.02 cm y^{-1}. The mean sedimentation rates derived with both methods are enhanced during the last ten years compared to previous values at the studied region by one order of magnitude, due to human implications. The activity concentration of the ^{238}U decay products does not exhibit variation along the depth. The activities of ^{226}Ra are enhanced (~30 %) compared to the activities of radon daughters (^{214}Pb, ^{214}Bi) especially at the surface layer. The results of the correlation between ^{232}Th decay products and ^{40}K indicate that there is positive correlation between their averaged activities. The good proportionality between ^{232}Th and ^{40}K concentrations may be attributed to the fact that thorium is a particularly insoluble element in water.

Keywords: Sedimentation rate; ^{137}Cs; ^{210P}b; Natural series radionuclides; ^{40}K; Thermaikos gulf; Northwest Aegean Sea

1. Introduction

The radiological study of sediments in coastal areas is of great interest for understanding the relation between human activities, hydrogeological and marine processes. The establishment

* Corresponding author.
Tel.: +30 -210- 772- 3783; *Fax*: +30 -210- 772- 3025; *E-mail address*: gelefthe@central.ntua.gr (G.Eleftheriou).

of a detailed composition profile and accurate chronology for sediments exhibits scientific priority for the marine environmental processes, like the origin of particulate matter, sediment mixing and deposition. For this reason, various applications have been developed the last years using natural radioisotopes as tracers for identifying and quantifying these processes [1]. Especially for the accumulation rates and sediment depositions estimation, many studies have been relished worldwide using as radiotracers the ^{210}Pb [2-4], the ^{137}Cs [5,6] or even the combination of both of them [7,8].

However, up to now natural radionuclides concentrations data from seabed sediments for the Greek Seas are very limited [9, 10] while totally absent for the North Aegean, where few water column data are available [11]. Only very recently, the sediment accumulation rate of Axios and Aliakmon River estuaries, located in the northeastern part of Aegean Sea, have been measured based on the concentrations of ^{137}Cs and ^{210}Pb in subsurface sediments located in front of the rivers mouths, with rate values varying from 0.180 to 0.883 cm/y [12]. These values are significantly increased compared to older estimations in the same region (0.02 – 0.05 cm/y), based on high-resolution seismic data [13].

In this work coastal sediments from the North Aegean Sea (Thermaikos Gulf) were analyzed for ^{137}Cs, ^{210}Pb and the characteristic radionuclides of the ^{238}U and ^{232}Th natural series to better understand the transport and the sedimentation process in a marine environment, which is strongly influenced by tense rivers flows, as well as to provide a baseline radionuclides concentrations dataset of the North Greece costal region. Core samples were also collected at different locations in order to perform sedimentation rate studies at the specific region.

2. Study area and methodology

The Thermaikos Gulf is located in the Northwest Aegean Sea having a length of 90 km and an average width of 30 km, while the exact sampling point is situated in the eastern part of the inner Gulf, near the "Makedonia" airport (Fig. 1). The sampling campaigns were conducted during December of 2005. The maximum depth of the sampled core that was reached was 50 cm. The sediments cores were taken to the laboratory and were kept in a temperature of -5 ^{o}C to ensure that the interstitial water remain at the corresponding level. Then the column sediments were sectioned into slices of 2 cm thickness and all samples were dried at 60 ^{o}C.

The samples were measured with 3 p-type coaxial High Purity Ge detectors (85 – 95 % relative efficiency) at the Low Background Facility of the Laboratori Nazionali del Gran Sasso (LNGS), located beneath 1400 m of rock that provides perfect shield against the cosmic rays. The shielding was further improved with lead layers (20 – 25 cm) having electrolytic copper in the innermost part (10 cm), while the measuring systems were continuously flushed with nitrogen in order to avoid any influence from the radon gas in the air. The energy and efficiencies calibrations were performed using a non commercial Monte Carlo simulation program (Jazzy) based on the GEANT4 software package [14], developed by the Laboratory's scientific stuff [15].The measurements had the same geometry for all detectors, with the samples placed at 10 mm from the detector window for 24 h. The ^{137}Cs and natural radionuclides activities of the samples were derived from the gamma ray spectrums using the SPECTRG spectrometry software package [16].

Especially for the ^{210}Pb measurements dried sediment samples (1-2 g) were attacked with HNO_3, HF, HCl and ascorbic acid – for the reduction of Fe^{3+} to Fe^{2+} – and the extracted isotopes where then deposited on silver discs. These disks were then placed between ZnS (Ag)

phosphor discs and both sides of the discs were measured with total alpha counters. The calibrations of the measuring systems were performed using standard samples (IAEA-414). The supported (background) ^{210}Pb activity was calculated from the averaged activities of the radon progeny gamma ray emitters and the unsupported (sample) ^{210}Pb specific activity was calculated subtracting the supported from the total ^{210}Pb specific activity.

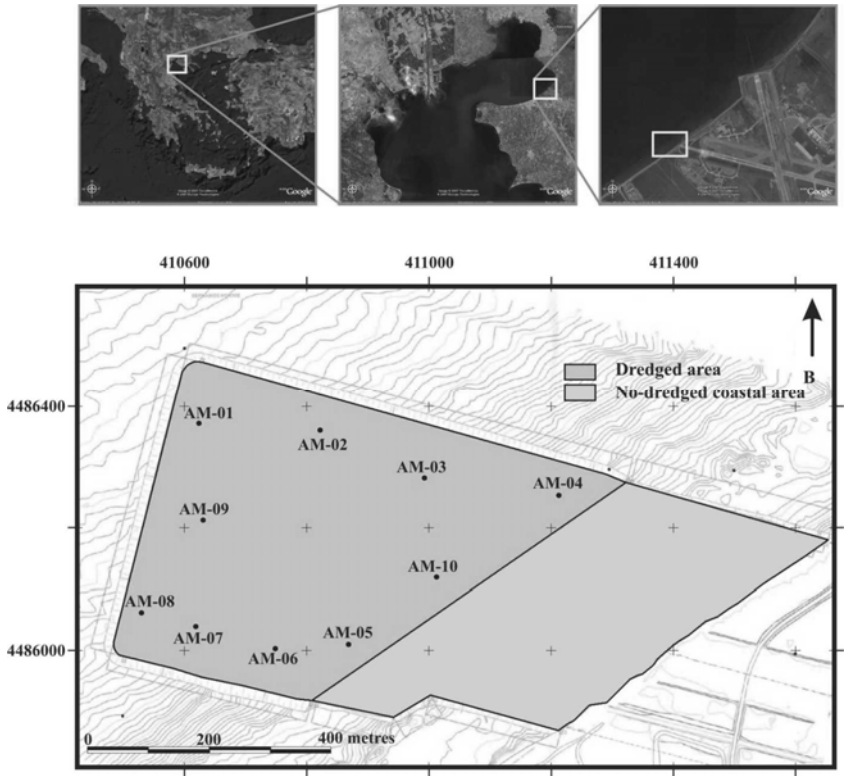

Fig. 1. A Map of Thermaikos Gulf at northwestern of Aegean Sea, Greece and horizontal view of the location of the sampled cores.

3. Results and discussion

The radiological study was carried out in order to enrich the database for the characteristic radionuclides concentrations in the seabed of the Aegean Sea, as well as for the estimation of the sedimentation rate in the region of the Thermaikos Gulf. The assessment of the sedimentation rate was done through empirical models using as tracers the ^{137}Cs and the ^{210}Pb isotopes.

3.1. Sedimentation rate

All examined samples were found highly enriched in ^{137}Cs (205 – 602 Bq/kg) and their sediment cores dating can be determined by interpreting the vertical profile of the anthropogenic ^{137}Cs activity. Anticipatingly, the first peak appearance of ^{137}Cs in the sediment cores retrieved from water bodies indicates the year of the Chernobyl accident (1986), while

the second peak occurrence indicates the year of maximum weapon testing fallout (1963). The identification of the ^{137}Cs photopeaks, subsequently can give an estimation of the mean sedimentation rate of each core, by assuming linear dependence between the two peaks along the depth of the core. The mean sedimentation rate is simply equal to the slope of the least squares linear fit between the two points.

A characteristic core analysis result is shown in the Figure 2. The sediment depth distribution for ^{137}C shows in general a typical peak concentration at around 4.5 cm followed by a monotone decline with depth. In addition another peak concentration is detected at around 9.5 cm. The sedimentation rate is calculated using the two peaks which correspond to Chernobyl accident (1986) and to atmospheric nuclear weapon testing (maximum fallout 1963) and varies from 0.2 to 0.3 cm/year.

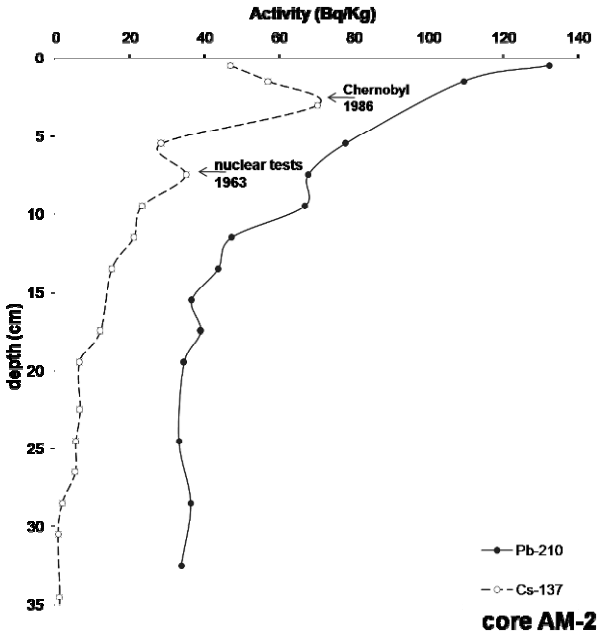

Fig. 2. The vertical distribution of the specific activity of ^{137}Cs and ^{210}Pb along with depth in AM2 core.

The unsupported ^{210}Pb activity (C) with depth is also used to calculate the sedimentation rates, according to the Constant Flux-Constant Sedimentation (CF:CS) model [17]:

$$C(z) = C_0 e^{-kz/r} \quad (1)$$

where C_o is the surficial unsupported specific activity (Bq/kg), k is the ^{210}Pb radioactive decay constant (0.03114 y^{-1}), z is the depth of sediment (cm) and r is the sedimentation rate of the core (cm/y).

The dependence of the logarithm of the unsupported ^{210}Pb specific activity with depth shows a linear dependence and the mean sedimentation rate is then calculated from the slope (k/r) of the fitted line. The mean sedimentation rate for the examined sediment cores (AM10

and AM2), varies from 0.23 to 0.27 cm/y, respectively, being in good agreement with the measured data using the ^{137}Cs method.

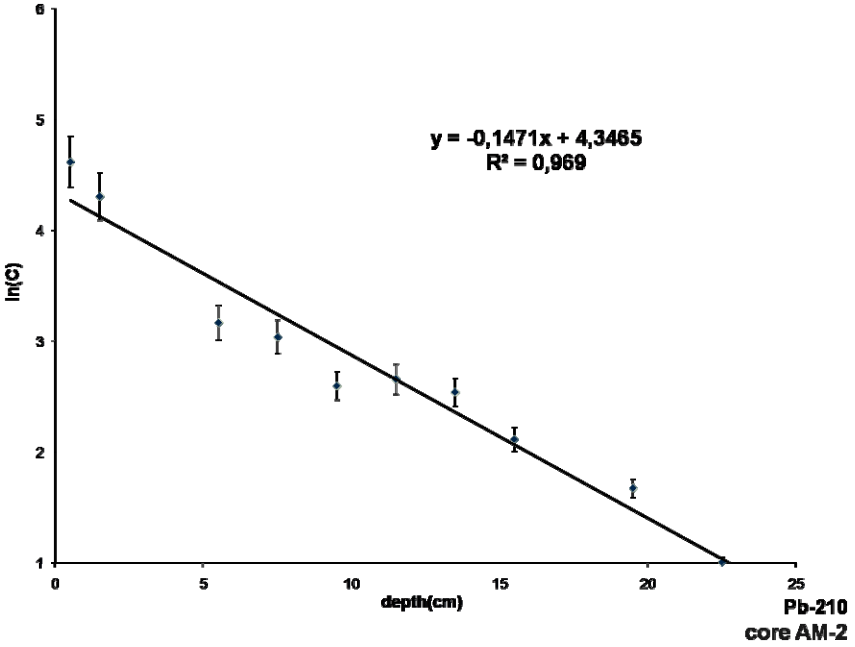

Fig. 3. A The logarithmic variation of the unsupported ^{210}Pb specific activity as a function of the depth of the sediment core AM2,with the liner fit of the experimental data.

3.2. Natural radionuclides series equilibrium

The main radionuclides that have been measured from ^{238}U (^{228}Ac, ^{212}Pb, ^{212}Bi) and ^{232}Th (^{226}Ra, ^{214}Pb, ^{214}Bi) natural series are the ones that can give detectible gamma photopeaks and are significant for the investigation of the equilibrium sustainability of these series. The activity concentration of the ^{238}U decay products does not exhibit variation along the depth. The activities of ^{226}Ra are enhanced (~30%) compared to the activities of radon daughters (^{214}Pb, ^{214}Bi). This can be interpretended as the effect of the radon loss throw the evaporation from the seabed to the sea water body.

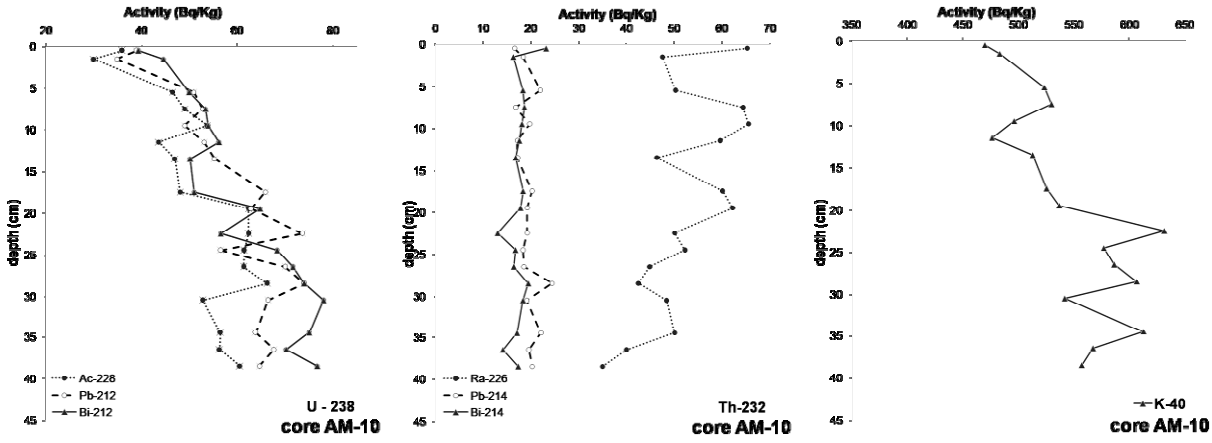

Fig. 4. The vertical activity distribution of ^{40}K radioisotope, ^{238}U and ^{232}Th natural series radioisotopes along with the depth in AM2 core.

The results of the correlation between ^{232}Th decay products and ^{40}K indicate that there is positive correlation between their averaged activities. The good proportionality between ^{232}Th and ^{40}K concentrations may be attributed to the fact that thorium is a particularly insoluble element in water.

4. Conclusions

The specific activities of ^{137}Cs were measured in Thermaikos Gulf at the surface as well as core sediments in order to provide us a baseline data regarding the coastal zone of the specific region. The mean surficial concentrations are elevated compared with recent data in the south, south-west and south east Aegean Sea (> 20 Bq/kgr). The granulometric and geotechnical properties of the harbor sediments seem to be correlated with this incensement due to river water mass transfer to the region.

Dating studies have been performed using ^{137}Cs as a tracer and the sedimentation rate varies from 0.2 to 0.3 cm/y. These results are in in good agreement with those calculated using ^{210}Pb as a tracer. The relative uncertainty is 4%, mainly due to the activity subtraction of the averaged activity of the radon progeny.

Measurements of the characteristic radionuclides of the ^{238}U and ^{232}Th natural series has been performed to better understand the transport and the sedimentation process in a marine environment, which is strongly influenced by the rivers at North Greece.

Acknowledgments

The research was supported by the Istituto Nazionale di Fisica Nucleare - Laboratori Nazionali del Gran Sasso (INFN-LNGS) in the framework of the "*Environmental Radioactivity Monitoring for Earth Sciences (ERMES) – Nuclear Spectrometer*" jointed research project between the Hellenic Centre for Marine Research (HCMR) and the Università degli Studi Roma III - Integrated Large Infrastructures for Astroparticle Physics (ILIAS) (contr. no. RII-CT-2004-506222).

References

[1] S. Krishnaswami, J.K. Cochran, U–Th Series Nuclides in Aquatic Systems, Radioactivity in the Environment, vol. 13, Elsevier, 2008.
[2] O. Radakovitch, S. Charmasson, M. Arnaud, P. Bouisset, Est. Coas. Shel. Res. 16 (1999) 363.
[3] A. Ugur, G. Yener, Appl. Rad. Isot. 55 (2001) 581.
[4] V.L.B. Sousa, C.A. Hazin, R.A. Lima, Nucl. Inst. Meth. Phys. Res. A 580 (2007) 690.
[5] S. Charmasson, Oceanol. Acta 26 (2003) 435.
[6] M. Frignani, D. Sorgente, L. Langone, S. Albertazzi, M. Ravaioli, J. Envir.Radioact. 71 (2004) 299.
[7] X. Lu, E. Matsumoto, Coast. Shel. Scien. 65 (2005) 83.
[8] C.M. Alonso-Hernadez, M. Diaz-Asencio, A. Munoz-Caravaca, (...), C. Crovato, Cont. Shel. Res. 26 (2006) 153.
[9] A.B. Cundya, I.S. Stewart, Tectonoph. 386 (2004) 147.
[10] H. Florou, G. Trabidou, G. Nicolaou, J. Envir. Rad. 93 (2007) 74.
[11] G.K.P. Muir, J.M. Pates, A.P. Karageorgis, H. Kaberi, Est. Cont. Shel. Res. 25 (2005) 2476.
[12] A.P. Karageorgis, H. Kaberi, N.B. Price, G.K.P. Muir, J.M. Pate, V. Lykousis, Cont. Shel. Res. 25 (2005) 2456.
[13] V. Lykousis, G. Chronis, Mar. Geol. 87 (1989) 15.

[14] S. Agostinelli, J. Allison, J. Amako, K. Apostolakis, J. Araujo, (…), D. Zschiesche, Nucl. Inst. Meth. A 506 (2003) 250.
[15] M. Laubenstein, personal communication, 2007.
[16] C.A. Kalfas, E. Tsoulou, Nucl. Instrum. Meth. A 500 (2003) 386.
[17] E.G. Goldberg, Proc. Radioactivity Dating Conf., Athens, 19-23 Nov., 1962; IAEA, Vienna (1963) 121.

Underground Low Flux Neutron Background Measurements in LSM Using a Large Volume ($1m^3$) Spherical Proportional Counter

I Savvidis[1], I Giomataris[2], E Bougamont[2], I Irastorza[4], S Aune[2], M Chapelier[2], Ph Charvin[2], P Colas[2], J Derre[2], E Ferrer[2], G Gerbier[2] , M Gros[2], P Mangier[2], XF Navick[2], P Salin[5], J D Vergados[6] and M Zampalo[3]

1 : Aristotle University of Thessaloniki, Greece
2 : IRFU, Centre d'études de Saclay, 91191 Gif sur Yvette CEDEX, France
3. LSM, Laboratoire Souterrain de Modane*, France*
4: University of Saragoza, Spain
5 : LSBB, France
6: University of Ioannina, Greece

Abstract: A large volume ($1m^3$) spherical proportional counter has been developed at CEA/Saclay, for low flux neutron measurements. The high voltage is applied to a small sphere 15mm in diameter, located in the center of the counter and the wall of the counter is grounded. Neutrons can be measured successfully, with high sensitivity, using ^{3}He gas in the detector. The proton and tritium energy deposition in the drift gaseous volume, from the reaction $^3He(n,p)^3H$, can provide the neutron spectra from thermal neutrons up to several MeV.

The detector has been installed in the underground laboratory in Modane (LSM) to measure the neutron background. The sphere has been has been filled with gas mixture of Ar + 2% CH_4 +3gr He-3, at 275 mbar. The thermal neutron peak is well separated from the cosmic ray and gamma background, permitting of neutron flux calculation. Other potential applications requiring large volume of about 10 m in radius are described in detail in reference

1. Introduction

The investigation on the large volume spherical proportional counter resulted in the development of a new neutron detector, based on the $^3He(n,p)^3H$ reaction[1]. The low background of the detector and the possibility to separate the γ ray pulses from the protons and alpha particle pulses increases the sensitivity on the neutron detection. The detector can successfully measure very low neutron fluxes
(10^{-6}n/cm^2/s, for thermal neutrons), providing the neutron energy spectrum from thermal up to several MeV at ground and underground level.

The large spherical geometry drift ($1m^3$), the good energy resolution (<2% FWHM with alpha particles at 5.5 MeV) and the simple read out (one channel reading) are some of the advantages of the detector. Other potential applications of this device requiring large volume are described in detail in reference [2,3,4,5,6,7].

2.The detector

The detector consist of a copper sphere, 1.3 m in diameter and 6mm thick (figure 1). The spherical vessel is well pumped (up to 10^{-8} mbar) and then is filled with a gas mixture at a pressure from several hundreds of mbars up to 5 bars. Out gassing in the order of 10^{-9} mbars/s is necessary for the amplification stability, because the present of the O_2 in the drift volume changes the detector characteristics.

A small stainless ball of 14 centimeter in diameter fixed in the center of the spherical vessel by a stainless steel rod (figure 2), acts as an electrode with positive high voltage and as a proportional amplification counter. The detector was operated with positive bias applied to the anode (inner sphere) while the cathode (external sphere) remained at ground potential. A high voltage capacitor was decoupling the high voltage cable to protect the sensitive preamplifier.

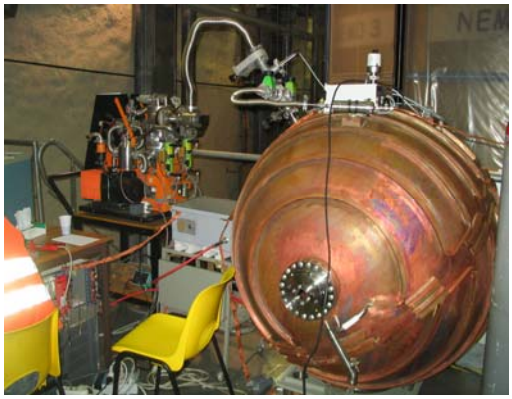

Figure 1. A photograph of the spherical vessel

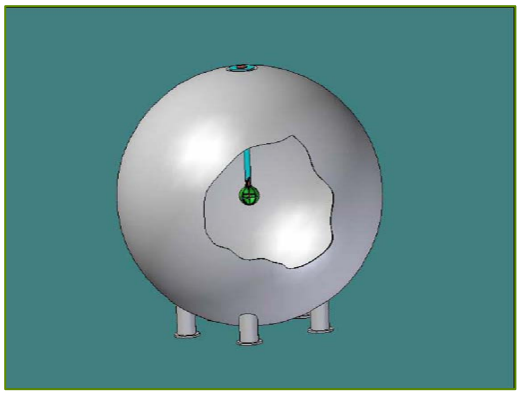

Figure 2. Sketch of the detector.

3. The electric field

The electric field in the drift volume plays a very important role for the proportionality and the energy resolution of the detector. The ideal detector is a spherical capacitor with perfect radical symmetric electric field. In a real implementation of the spherical TPC concept, the ideal spherical symmetry is broken by the rod that supports the central electrode and that necessarily connects it to the front-end electronics, placed outside, to amplify and read the signals. In figure 3 the equipotential lines are plot for this simplest geometry, showing how the presence of this rod makes the electric field to be far from spherically symmetric. It means that the amplification depends on the direction and the position of the track of a charge particle in the drift volume and makes impossible the energy resolution.

To solve the problem of field distortion due to voltage anode electrode, a cylinder around the high voltage rod, placed at 4 mm away from the central sphere and powered with an independent voltage V_2 (which can be zero, i.e., at ground). The equipotential lines for the described "corrected" configuration are shown in figure 4.

Energetic charged particles, x-rays, or gamma rays or even neutrons entering the detector strip electrons from the gas atoms to produce positively charged ions and negatively charged electrons. The electric field created across the electrodes drifts the electrons to the positive electrode. Near the inner anode sphere the electric field is high enough and electrons gain enough energy to ionize more gas atoms, a process that produces more electrons. Typical gases at atmospheric pressure required field strength on the order 10kV/cm to produce the avalanche of secondary electrons around the small anode ball. The avalanche is produced at a few mms distance from the anode and the positive ions drifting toward the cathode are inducing a pulse to the charge preamplifier. Since the avalanche takes place near the small ball and the electrons are attracted to it the positive ions travel a much greater distance. Therefore the induced pulse to the preamplifier is mainly due the ion movement; electrons produced during avalanche process have a negligible contribution to the signal.

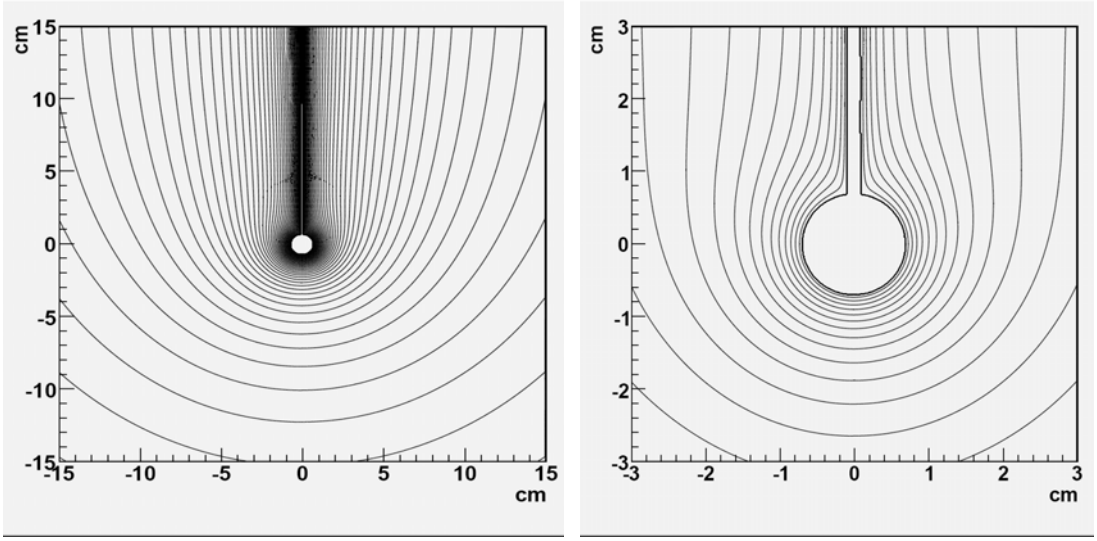

Figure 3. The epuipotential lines around the 14 mm sphere without any correction.

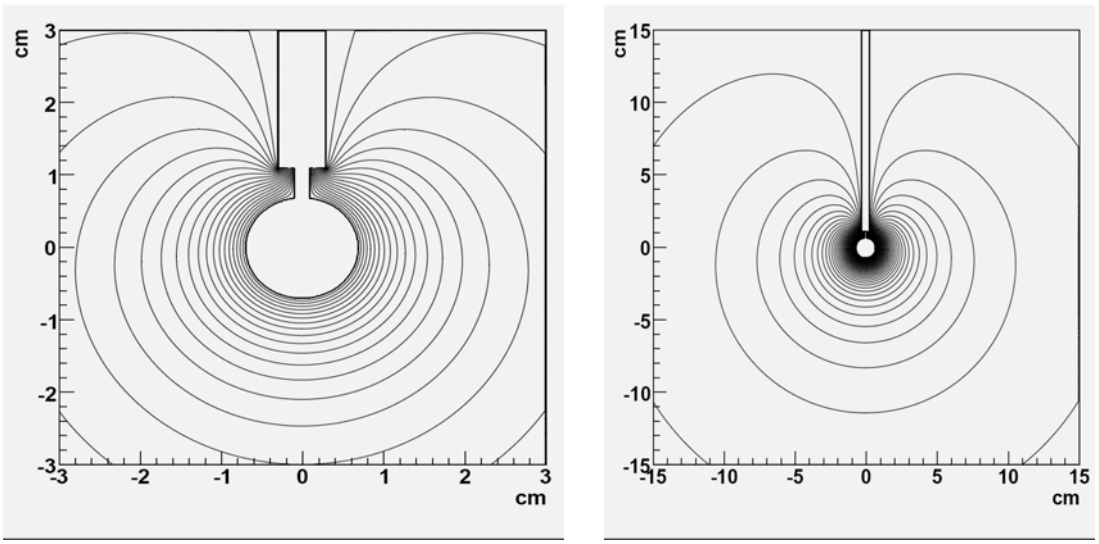

Figure 4. Electrostatic configuration for the readout electrode, with the "corrector"

4. The energy resolution

The energy resolution of the detector has been tested using ^{222}Rn gas and detecting the alpha particles from ^{222}Rn and ^{222}Rn daughters. Since the ^{222}Rn gas cover homogenously all the drift volume of the detector, we have alpha emission in every direction and in all the positions of the detector. The gas mixture consist of Ar (98%) and CH4(2%) at pressures, from 150 mbars up to 1 bar. The high voltage vary from 1.5 kV up to 5 kV depending on the gas pressure. In the figure 5 is shown the peaks observed from a ^{222}Rn radioactive source. From left to right we observe the ^{222}Rn peak at 5.5 MeV, the ^{218}Po and ^{214}Po at 6.0 MeV and 7.7 MeV respectively. The energy resolution was 2% FWHM at 200 mbar gas pressure and 2.8 kV High Voltage.

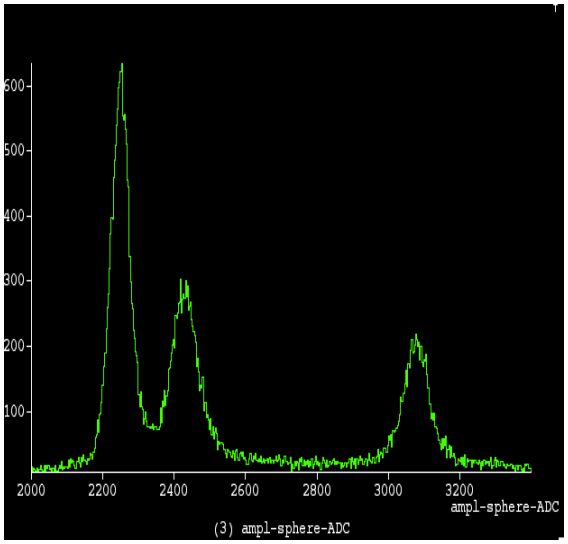

Figure 5. The peaks observed from a ^{222}Rn radioactive source. From left to right we observe the ^{222}Rn peak at 5.5 MeV, the ^{218}Po and ^{214}Po at 6.0 MeV and 7.7 MeV respectively.

5. The thermal neutron flux in the LSM

In the present work we have been used the ^{3}He gas as converter for thermal and fast neutron detection up to several MeV. Neutrons interact with ^{3}He as follows, $n+^{3}He \rightarrow p+^{3}H+765$ keV. The signal is the sum of the p and ^{3}H energy deposition in the drift volume and depends on the neutron energy. In the case of thermal neutrons we measure one peak 765 keV and for the fast neutrons the energy peak is En + 765 keV, were En is the fast neutron energy.

The detector has been installed in the LSM, to measure the underground neutron flux. The gas mixture was Ar +2% CH4 at p=280 mbar with 3 gr of He-3. Thermal neutron capture rate was 0.0048 evts/s = 417 evts/d and the thermal neutron flux was Φ_{th}=1.9 10^{-6} n/cm^2/s. In the figure 6 is shown the thermal neutron peak after rise time cut.

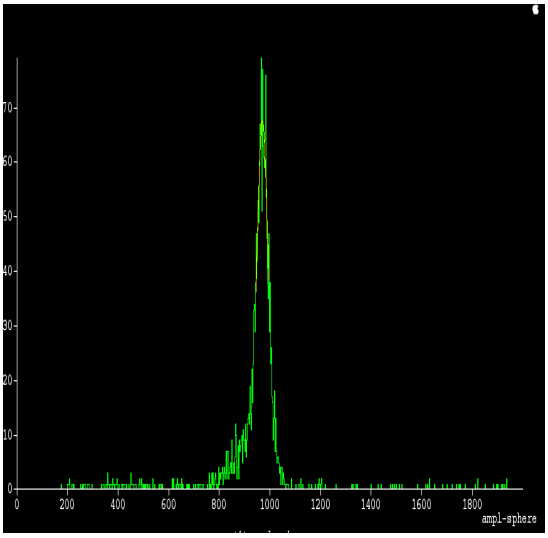

Figure 6. The thermal neutron peak after rise time cut.

6. Conclusions

The spherical proportional counter is a high sensitivity neutron detector. The sensor is stable for long time measurements and the decrease in gain is small (≈ 0.2% per day). The detector can measure low fluxes of the underground thermal neutrons and the seasonal variation of the flux.

REFERENCES

[1] I. Giomataris et al., JINST 3:P09007,2008.
[2] I. Giomataris and J.D. Vergados, Nucl.Instrum.Meth.A530:330-358,2004
[3] I. Giomataris *et al.* Nucl.Phys.Proc.Suppl.150:208-213,2006.
[4] S. Aune *et al.*, AIP Conf.Proc.785:110-118,2005.
[5] I. Giomataris and J.D. Vergados, Phys.Lett.B634:23-29,2006.
[6] J. D. Vergados et al., Phys.Rev.D79:113001,2009.
[7] A. Dedes et al., arXiv:0907.0758